GENETICS

Chromatin conformation, gene transcription, and nucleosome remodeling as an emergent system

Luay M. Almassalha[1,2], Marcelo Carignano[2,3]†, Emily Pujadas Liwag[2,4]†, Wing Shun Li[2,3,5]†, Ruyi Gong[2,3]†, Nicolas Acosta[2,3]†, Cody L. Dunton[2,3]†, Paola Carrillo Gonzalez[2,3]†, Lucas M. Carter[2,4]†, Rivaan Kakkaramadam[2,4]†, Martin Kröger[6]†, Kyle L. MacQuarrie[7,8]†, Jane Frederick[2,3]†, I Chae Ye[2,3]†, Patrick Su[2,3], Tiffany Kuo[2,4], Karla I. Medina[2,4], Josh A Pritchard[2,3], Andrew Skol[7], Rikkert Nap[2,3], Masato Kanemaki[9,10,11], Vinayak Dravid[5,12,13,14,15], Igal Szleifer[2,3,12]*, Vadim Backman[2,3]*

In single cells, variably sized nanoscale chromatin structures are observed, but it is unknown whether these form a cohesive framework that regulates RNA transcription. Here, we demonstrate that the human genome is an emergent, self-assembling, reinforcement learning system. Conformationally defined heterogeneous, nanoscopic packing domains form by the interplay of transcription, nucleosome remodeling, and loop extrusion. We show that packing domains are not topologically associated domains. Instead, packing domains exist across a structure-function life cycle that couples heterochromatin and transcription in situ, explaining how heterochromatin enzyme inhibition can produce a paradoxical decrease in transcription by destabilizing domain cores. Applied to development and aging, we show the pairing of heterochromatin and transcription at myogenic genes that could be disrupted by nuclear swelling. In sum, packing domains represent a foundation to explore the interactions of chromatin and transcription at the single-cell level in human health.

INTRODUCTION

Even as the tools to probe genome structure and function have rapidly advanced, the conceptual framework around structure-function has converged on the dichotomy between open (transcriptionally active, low-density, euchromatin rich, A compartment) and closed (transcriptionally repressed, high-density, heterochromatin rich, B compartment) states (*1*–*8*). There are several prominent models centered around this framework: loop extrusion as a barrier element of epigenetic spreading (*9*, *10*), self-attraction of nucleosome markers producing segregation (*11*–*14*), and hierarchical functional assemblies (*5*, *15*, *16*). The central goal of all these models is explaining how the partitioning of the 2-m-long human genome into nuclei several microns in diameter produces structures that can effectively regulate the nuclear processes crucial for cell function: transcription, replication, and DNA repair.

At the level of transcription, these models all face a formidable challenge: Dichotomizing the genome into two distinct groups simply does not account for the patterns in expression that are observed when chromatin is induced to transform from one state to the other (*6*, *7*, *17*–*19*). Specifically, inhibiting heterochromatin enzymes does not result purely in transcriptional activation (*17*–*19*). Related to this paradox are the complexities observed in compartments and subcompartments in high-throughput conformation capture (Hi-C). Ever since the early descriptions, compartments defied a pure delineation into active and inactive nucleosome posttranslational modifications (*6*, *7*). For example, as observed by Rao *et al.* (*7*), repressive histone markers such as histone 3 lysine 9 trimethylation (H3K9me3) can be as strongly correlated with transcriptionally active A2 subcompartments as transcriptionally active markers such as H3K4me3 (*7*). Likewise, the correlation of H3K9me3 is comparable to those of euchromatin marks in B subcompartments (*7*). Analogous to these limitations, gene expression cannot be predicted solely on the basis of the combinatorial presence of histone marks or accessibility at gene loci (*20*–*22*). These limitations become more pronounced when considering that inhibition of loop extrusion by RAD21 depletion has muted impacts on gene transcription even as H3K9me3 increases as measured by chromatin immunoprecipitation sequencing (ChIP-seq) (*23*). Compounding this problem, the loss of RAD21 has no discernable impact on the amount of heterochromatin within spatially resolved chromatin aggregates observed on super-resolution imaging (*24*). Collectively, these findings demonstrate that ensemble connectivity features alone may not translate into space-filling conformations due to potential differences between genome topology and chromatin conformation. Whereas topological properties such as topologically associated domains (TADs) are ensemble properties of thousands of cells (*6*, *7*), chromatin conformation describing the chromatin polymer at the level of an individual cell is not merely the observed connections. Therefore, integrating the concepts of transcription, accessibility, nucleosome modification, and loop extrusion into a cohesive system remains elusive.

[1]Department of Gastroenterology and Hepatology, Northwestern Memorial Hospital, Chicago, IL 60611, USA. [2]Center for Physical Genomics and Engineering, Northwestern University, Evanston, IL 60208, USA. [3]Department of Biomedical Engineering, Northwestern University, Evanston, IL 60208, USA. [4]Interdisciplinary Biological Sciences Graduate Program, Northwestern University, Evanston, IL 60208, USA. [5]Applied Physics Program, Northwestern University, Evanston, IL 60208, USA. [6]Magnetism and Interface Physics and Computational Polymer Physics, Department of Materials, ETH Zurich, CH-8093 Zurich, Switzerland. [7]Stanley Manne Children's Research Institute, Ann and Robert H. Lurie Children's Hospital of Chicago, Chicago, IL 60611, USA. [8]Northwestern University Feinberg School of Medicine, Chicago, IL 60611, USA. [9]Department of Chromosome Science, National Institute of Genetics, Mishima, Shizuoka 411-8540, Japan. [10]Graduate Institute for Advanced Studies, SOKENDAI, Yata 1111, Mishima, Shizuoka 411-8540, Japan. [11]Department of Biological Science, The University of Tokyo, Bunkyo-ku, Tokyo 113-0033, Japan. [12]Department of Chemistry, Northwestern University, Evanston, IL 60208, USA. [13]Materials Science and Engineering, Northwestern University, Evanston, IL 60208, USA. [14]Northwestern University Atomic and Nanoscale Characterization Experimental (NUANCE) Center, Northwestern University, Evanston, IL 60208, USA. [15]International Institute for Nanotechnology (IIN), Northwestern University, Evanston, IL 60208, USA.
*Corresponding author. Email: igalsz@northwestern.edu (I.S.); v-backman@northwestern.edu (V.B.)
†These authors contributed equally to this work.

A potential solution to this challenge is to start with the observed structure of chromatin on nanoscale imaging techniques and then solve the inverse problem. There is broad consensus that the smallest functional physical structure of chromatin is nucleosomes organized as "beads on a string" or clutches (5 to 25 nm) (*25*). Above this scale, however, there is limited consensus. Using a variety of methods and contrast agents which include but are not limited to chromatin electron microscopy (ChromEM) (*25*), structured illumination (SIM) (*24*, *26*, *27*), single-molecule localization microscopy (SMLM) (*28*), live-cell spectroscopic nanoscopy (*29*), and DNA paint (*26*, *30*–*32*), supra-nucleosome organization has been described as variably sized structures such as nucleosome clutches comprising a small number of nucleosomes (*33*), TAD-like domains (200 to 500 nm) (*30*, *31*), nanodomains (100 to 200 nm) (*26*), chromatin fibers (50 to 200 nm) (*34*), chromatin domains (100 to 200 nm) (*24*, *35*), and packing domains (PDs; 50 to 200 nm) (*29*). In this work, we tested an intriguing hypothesis to resolve the paradoxical behavior of transcription upon heterochromatin enzyme inhibition while linking these structures into a cohesive framework. Specifically, we hypothesized that the observed physical properties of ChromEM-resolved PDs reflect their structure-function life cycle with respect to gene transcription: (i) Small, low-density (nascent) domains are formed by processes such as cohesin-mediated loops and RNA polymerase–mediated promoter-promoter/promoter-enhancer interactions. (ii) The size of nucleosome remodeling enzymes results in preferential penetration of heterochromatin enzymes in areas of high density within domain cores to mature the structure. (iii) The produced density near domain boundaries provides an optimal physical scaffold for RNA synthesis by stabilizing the binding of the polymerase and transcription factors within intermediate densities. The result is that chromatin is not organized into two distinct groups but into a unified, dynamic domain-forming system.

Collectively, this work demonstrates that (i) chromatin in vitro assembles into PDs independent of the cell line. (ii) PDs are heterogeneous with a broad distribution of sizes, density, and packing efficiencies that reflect their function. (iii) The act of gene transcription and cohesin-mediated loop extrusion facilitates the formation of nascent PDs, but this is insufficient for maturation to occur. (iv) Transcription, enzymatic size, density, and divalent ionic concentrations mechanistically maintain domain stability. (v) PDs do not appear to be the physical manifestation of TADs. (vi) Optimal gene transcription depends critically on domain stability. We conclude by showing how the disruption of domain self-assembly from physical considerations can have physiologic consequences by modeling how nuclear swelling would disrupt myogenic domains with a focus on sarcopenia (deleterious loss of muscle mass). Given that sarcopenia is independently associated with all-cause adult morality and quality of life, understanding domain transformation can provide a mechanistic link between physical genomic organization, gene transcription, and human disease.

RESULTS

Chromatin PDs are the predominant supra-nucleosome nuclear structure

The pioneering work by Ou *et al.* (*25*) described the capacity to proportionally label DNA using a photoactivatable dye (DRAQ5) and click chemistry of diaminobenzidine (DAB) that results in specific staining of DNA on electron microscopy (ChromEM) (*25*). This approach overcomes a major prior limitation in ChromEM, as in prior studies the nonspecific binding of contrast resulting in binding to chromatin and nonchromatin molecules. Using ChromEM, it was shown that individual DNA fibers and nucleosome assemblies form as disordered nucleosome clutches (5 to 25 nm) (*25*). To extend the capabilities of ChromEM technologies to higher-order structures, we developed scanning transmission chromatin electron microscopy (ChromSTEM) with high-angle annular dark-field tomography. In ChromSTEM tomography, the mass density of DNA is proportional to the intensity with a resolution of ~2 nm. Although ChromSTEM tomography is the only method capable of resolving the ground-truth physical structure of chromatin, the throughput is limited, and it is not now possible to delineate DNA density at specific genes. By pairing ChromSTEM with other modalities as described below, some of these limitations can be overcome. Using ChromSTEM tomography, we demonstrated that chromatin forms into higher-order structures from these disordered nucleosome fibers (<25 nm) by folding into heterogeneously distributed PDs (50 to 200 nm) and lastly converging into space-filling territories (>200 nm) (*29*, *36*). Physically, PDs are heterogeneous power-law chromatin assemblies with a distribution of densities, sizes, and folding properties.

Several properties of PDs are obtained with ChromSTEM tomography: average density also known as the chromatin volume concentration (CVC), domain size (radius, r), the polymeric filling of chromatin within the domain as quantified by the mass fractal dimension, D, and the packing efficiency (how efficiently nucleic acids fill the domain volume) (*36*). While domain radius and CVC are relatively intuitive properties (how large and how dense a domain is, respectively), fractal dimension and packing efficiency are not frequently described metrics of chromatin biology. However, these properties are crucial to translate how the polymeric structure of chromatin intersects with the occupied volume, as described below.

Consider a segment of the genomic length, L, e.g., 100 kbp, composed of nucleosome monomers linked together by DNA. Although each nucleosome likely has slight variations in DNA content, for simplicity, it is reasonable to assume that these contain ~200 bp. This would produce a linear segment of ~500 nucleosomes. Contact probability between monomers decays as a function of the segment length if no constraints are present with contact scaling S, a metric used in polymer models and experimental methods such as Hi-C (*6*, *9*, *37*, *38*). This indicates that adjacent nucleosomes on this segment are more likely to be in contact than those further away (e.g., nucleosome 250 is more likely to contact the 240/260 positions than the 100/400 positions). This same segment of chromatin has an accompanying total number of nucleotides, M, that occupies a domain volume with radius, r, by the mass-to-distance relationship, $M(r) \propto Ar^D$. Packing efficiency, A, is a complementary measurement that ranges between 0 and 1, where 1 indicates that the domain volume is optimally filled (*36*).

Independent of the cell line (A549, HCT-116, and CRL-2522 fibroblasts), we observed that PD formation occurs (Fig. 1A and movie S1) with distinct distributions in D (Fig. 1B), domain radius (Fig. 1C), CVC (Fig. 1D), and packing efficiencies (Fig. 1E). In the majority of cases, the domains had $D > 2$. Visually, PDs have a high-density interior that decays to a low-density exterior (Fig. 1F and fig. S1) in all tested models, until the emergence of the transition to interdomain areas (Fig. 1G) with CVC decreasing as a function of distance r from the domain center as CVC $\propto A / r^{3-D}$, a relationship

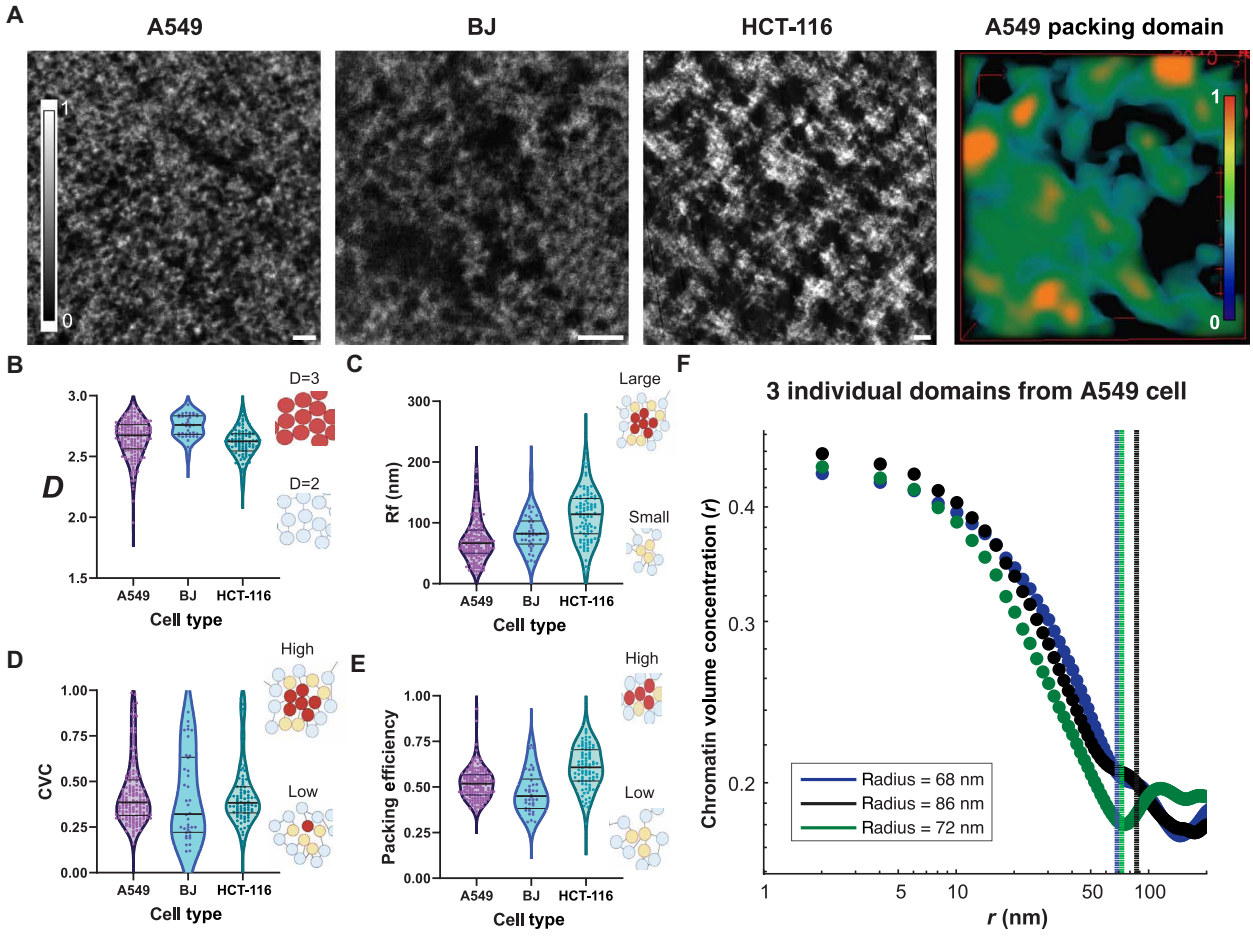

Fig. 1. PDs are the predominant supra-nucleosome structure independent of the cell line. (**A**) High-resolution mean projection from ChromSTEM in A549, BJ, and HCT-116 cells with a representative domain tomogram from the A549 cell. Scale bars, 200 nm. Domain size, 200 nm by 200 nm. (**B** to **E**) Analysis of structural properties of domains for these distinct cell types demonstrates heterogeneity of domain structures by cell type. (B) Scaling of chromatin packing ranges between two and three in all cell types. (C) Domain radius typically range from 50 to 200 nm between all cell lines. (D) Variations in CVC within domains are observed. (E) Quantification of chromatin packing efficiency. (**F**) Representative spatial distribution of density from domain interiors toward their periphery demonstrates a conserved, power-law geometry with a decay to the average nuclear density at the periphery. Domain boundary for blue (68 nm), black (86 nm), and green (72 nm).

that follows from the mass scaling above and confirmed via ChromSTEM. The CVC at domain edges typically approaches ~20% (Fig. 1G), indicating domains transition not from high density to very low density but toward intermediate physical conditions. A remarkable feature of domains is that they defy discrete binarization into high-density and low-density structures. As a result, domains do not appear to represent assemblies of two distinct chromatin phases but a continuous distribution of states. Consequently, these domains are best defined not by high internal density but by the power law scaling internal conformation of the chromatin polymer, i.e., conformationally defined domains.

Pairing the information of domain size and packing efficiency, we hypothesized that although ChromSTEM imaging is performed on fixed cells, in principle, the cross section of observed domains provides information on their lifecycle. Specifically, we hypothesized that high packing efficiency could be consistent with mature domains; large, low packing efficiency domains could be consistent with decaying domains; and small, low packing efficiency domains could be consistent with newly forming (nascent) domains. Collectively, this suggested that domains existed in a unified, dynamic domain-forming system, but this could not be delineated with electron microscopy experiments alone. As explored below, pairing domain states with molecular interactions requires integration of mathematical modeling, polymer simulations, and nanoscale molecular imaging.

Long-range chromatin interactions, nuclear density, excluded volume, and ionic interactions influence the structure of domains

Since domains did not separate into two dichotomous groups, we next considered what processes could produce a continuous distribution of structures. To do so, we turned to polymer modeling. The simplest polymer model of a chromatin segment is a random walk (Fig. 2A). Each nucleosome monomer is linked by a fixed distance, and two nucleosomes cannot occupy the same space (Fig. 2A). An interesting observation of this model is that, without any other

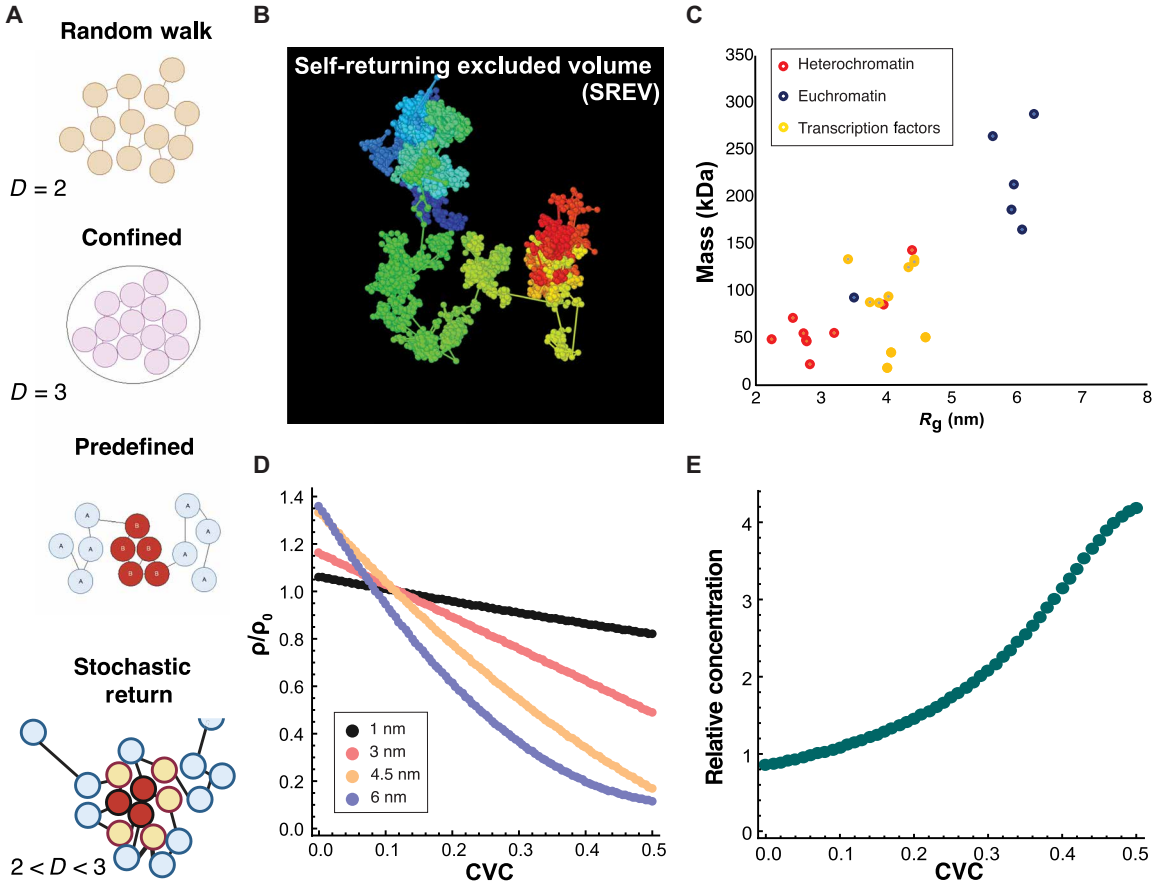

Fig. 2. Stochastic returns and excluded volume influence domain interactions with remodeling enzymes. (**A**) Schematic representation of modeling frameworks in chromatin. A random walk and a confined random walk are cases of nucleosomes with fixed distances. In both cases, the produced structure results in a limiting case of chromatin domains with a $D = 2$ (random walk) and $D = 3$ (confined random walk or fractal globule). Forced attractions can produce more complex structures, but the discrete partitions result in two separated structures (low density, A; high density, B states). Stochastically forced returns that depend on the distance between the nucleosomes produce corrugated, mass-fractal structures that resemble ChromSTEM-resolved domains. These have a continuous decrease in density from high-density cores (red) to intermediate conditions (yellow) and lastly to outer zones (blue) before transition to interdomain space. (**B**) Representative chromosome fragment from SR-EV demonstrating the formation of chromatin PDs due to the intersection of stochastic return events and the excluded volume of monomers (nucleosomes). (**C**) The molecular mass in kilodaltons versus the radius of gyration, R_g, in nanometers predicted from AlphaFold configurations organized by enzyme function (red, heterochromatin; yellow, transcription factors; blue, euchromatin). Euchromatin enzymes have a radius that is approximately twice the size of heterochromatin enzymes, $P < 0.001$. (**D**) Simulated protein penetration relative to the average penetration as a function of size demonstrating preferential localization of larger enzymes to low-density regions (CVC < 0.1) and small molecules minimally affected by higher CVC. (Black, 1-nm radius, small molecule. Red, 3-nm radius, heterochromatin protein. Yellow, 4.5-nm radius, transcription factors. Blue, 6-nm radius, euchromatin protein). (**E**) Molecule size results in differential localization as a function of domain CVC in SR-EV configurations with increased relative concentration of smaller molecules to domain interiors (3-nm heterochromatin versus 6-nm euchromatin enzyme is shown).

constraints, it can only statistically produce a fractal dimension of $D = 2$. This is a consequence of the Central Limit Theorem: The sum of N steps with independent jump vector distributions having a finite expectation and a variance is normally distributed with the variance proportional to N; this ensures that the spatial extent of the random walk (e.g., the radius of gyration) scales as $\sim N^{1/D}$ with $D = 2$ (*37*). In contrast, most PDs observed using ChromSTEM have $2 < D < 3$. Several modifications have been attempted to overcome this limitation. One approach is to produce physical confinement, which produces the fractal globule which is a limiting case where $D = 3$ (Fig. 2A) (*6*, *37*). In both approaches, it is not possible to produce the domain states observed on ChromSTEM while maintaining the visually apparent corrugation (gaps between domains; Fig. 1A). An alternative strategy is to apply attractive potentials between different monomer segments (A attracts A, and B attracts B), but this would require a priori segment information and produce dichotomous segments without a continuous mass density decay (Fig. 2A) (*9*, *11*–*13*, *38*–*41*).

We previously described an alternative approach centered on the concept of a stochastically returning random walk (SRRW) (*42*). In SRRW, "returns" are a mathematical concept stating that a segment has a probability, p, of returning to a prior point and a probability $1\text{-}p$ of taking a forward step to a subsequent point. In SRRW, step sizes are not a single fixed distance. Instead, the size of any step was modeled as an inverse power law distribution where short steps were more likely, but long steps still rarely occurred. Last, the likelihood of a return or forward step itself depended on the distance traversed in the current step. The longer the current step, the less likely for a return to occur (Fig. 2, A and B). The main limitation in SRRW is that the segments do not occupy a physical volume (they

are dimensionless). In SRRW, therefore, segments cannot interact with one another, chromatin remodeling enzymes, or polymerases. In SRRW, crucial physical attributes, such as the nuclear volume, do not affect the nodes and branches (*42*). We addressed this limitation recently by turning this mathematical framework into a polymer model where each segment was modeled as a nucleosome disk, the so-called stochastic returns with excluded volume (SR-EV) model (Fig. 2, A and B) (*42*). SR-EV retains the mathematical framework of SRRW, but since the segments are now space-filling nucleosomes, it is easier to interpret what steps and returns represent in the context of biological processes and chromatin structures.

In eukaryotic nuclei, a nucleosome can interact with neighboring nucleosomes due to a combination of short- and long-range processes. These include the activity of heterochromatin- and euchromatin-modifying enzymes, nucleosome-nucleosome bridging [e.g., heterochromatin protein 1 (HP1) cross-linking], cohesin extrusion (*23*, *43*, *44*), transcription-mediated promoter-promoter (P-P) interactions (*28*, *41*), promoter-enhancer (P-E) interactions (*43*), and stochastic contacts from confinement of the genome in three-dimensional (3D) space (*45*). The distribution of steps produced by these factors implicitly enters into the model at the level of the steps and returns produced. Some processes (loop extrusion, P-P, and P-E) are unique in that they may produce forced long returns, but it is not necessary to explicitly define the position of forced returns to reproduce the domains observed on ChromSTEM. This SR-EV has a remarkable degree of quantitative and qualitative agreement with domains observed on ChromSTEM (Fig. 2B) (*46*), recapturing the distribution of sizes, CVC, and *D* values (*46*). As we explore below, when pairing these considerations with the physical properties of nucleosome remodeling complexes (heterochromatin enzymes are small, euchromatin enzymes are large), it has profound implications on the role of domains in transcriptional reactions.

It is immediately clear that without predefining monomer-monomer attractive forces or fixed loop extrusion as barrier elements, SR-EV creates the domain structures observed above in Fig. 1 (*46*). Two critical features from SR-EV and ChromSTEM tomography (Figs. 1 and 2) are immediately evident: (i) Domains are the predominant chromatin physical structure, and (ii) they are not produced by dichotomous segmentation into hetero- and euchromatin. An approach with dichotomous segmentation would not produce the continuous, mass-fractal behavior of domains (density gradually decaying from the center as an inverse power law of the radial distance $\propto 1/r^{3-D}$) with $2 < D < 3$ but would instead create discrete partitions. Instead, stochastically encoded forced returns are necessary for domains to form with the experimentally observed geometry. The fact that forced returns are critical for domains to form is evident from the Central Limit Theorem for dependent random variables: Forced returns result in anticorrelation between steps that might be separated even by a large linear distance *N*. This results in an attenuated dependence of the variance of the sum of *N* steps as a function of *N*. While in the absence of forced returns, the spatial extent of a random walk $\sim N^{1/2}$, forced returns allow for the $\sim N^{1/D}$ scaling with $D > 2$. In the absence of such a process, mass-fractal domains will not form (Fig. 2A).

Since forced returns may generate nascent domains, it is worth now considering the structure of nucleosome remodeling complexes, cohesin subunits, and RNA polymerases. All of these are known to be multisubunit protein complexes, and as such, they also occupy space in the nucleus. While it is difficult to know whether these multisubunit complexes assemble in situ onto DNA sequences or are preassemble within the cytoplasm, as a first approximation, we investigated the effect of enzymes size in how it interacts with domains.

Building on the excluded-volume concepts introduced by Matsuda *et al.* (*47*), Putzel *et al.* (*48*), Maeshima *et al.* (*49*), and Miron *et al.* (*24*) in chromatin, molecular size can define what areas are accessible and inaccessible. This principle is widely used in molecular biology techniques like Western blots where a 1-nm protein can more easily and quickly traverse the gel than a 10-nm protein when subjected to an electric field with equivalent charges. In contrast to a gel, chromatin domains are heterogeneous structures and can undergo chemical reactions with the molecules they interact with (e.g., transcription). Using AlphaFold, we converted protein mass for these nuclear enzymes into approximate protein sizes (*50*). From the AlphaFold-predicted configurations of heterochromatin enzymes, euchromatin enzymes, and transcription factors, we calculated the radius of gyration (R_g) of each protein and found that, on average, euchromatin enzymes were significantly larger than heterochromatin enzymes (R_g of ~5.5 nm in comparison to ~3 nm) (P value < 0.001; Fig. 2C and table S1) with enhancer of zeste homolog 2 (EZH2) (R_g of 3.95 nm) which catalyzes the formation of H3K27me3 as an interesting outlier.

Using configurations generated by SR-EV, we measured the relative penetration of a 1.5-nm small molecule, a 3-nm "heterochromatin" protein, a 4.5-nm transcription factor, and a 6-nm "euchromatin" protein as a function of domain density. This intrinsic property when paired with SR-EV configuration results in spatial preferences of larger, euchromatin proteins to the domain periphery with preferential localization of smaller heterochromatin proteins to the dense domain interiors (Fig. 2D). Heterochromatin enzymes were much less likely to be found at the periphery of domains, with a fourfold abundance in their relative concentrations at high-density interiors compared to euchromatin ones (Fig. 2E). The RNA polymerase core subunit has an R_g of ~5 nm that is comparable to euchromatin enzymes (tables S1 and S6). It would likely localize in the interdomain space when it is inactive. However, a crucial attribute of transcriptional machinery is that it operates best with an intermediate degree of crowding. This occurs from competition between the entropic gain of the polymerases remaining bound to DNA during intermediate reactions and the diffusion rates of the reactants. The low chromatin density outside of a domain increases the diffusion rates of transcriptional reactants at the expense of their binding constants; the high-density chromatin cores are inaccessible to most reactants, whereas the "ideal" conditions at the intermediate periphery of a mature domain optimize both rate-limiting processes (diffusion, intermediate reaction complex stability) due to the excluded volume effects (*47*, *51*–*53*). As such, the optimal conditions for transcription reactions are not on the outer zone but within an intermediate ideal physical zone (*29*, *47*, *52*–*54*).

Last, a consideration that arises from the observation of high-density centers within domains is the regulation of the electrostatic charges from the large concentration of DNA within domain interiors. Functionally, the posttranslational modification of histone proteins helps to buffer these charges in conjunction with the local ion concentrations (Na^+, K^+, Ca^{2+}, Mg^{2+}, etc.) (*55*–*57*). As such, manipulation of ion concentrations would also be expected to exert an effect on domain stability with the loss of divalent ions (Ca^{2+} and Mg^2) anticipated to result in domain collapse.

A phenomenological model of chromatin domain self-assembly

Motivated by these observations, we hypothesized that a framework based on the domain life cycle could explain the paradox of why inhibiting heterochromatin enzymes can disrupt transcription. We postulated that the domain life cycle depended on three rules that intersected with transcriptional reactions. (i) Long steps from a forced return (cohesin, P-P, and E-P interactions) create nascent domains. This occurs because a local density pocket is formed that results in some preferential positioning of hetero- and euchromatin enzymes but not to the extent observed in mature domains. (ii) Domain maturation depends on the preferential localization of enzymes within centers, ideal zones, and peripheries. Maturation is not guaranteed to happen from a nascent domain unless a critical mass is initially reached to produce the preferential position of hetero- and euchromatin enzymes. (iii) Transcription accelerates at the formed ideal physiochemical zone due to the stabilization of the intermediate complexes (Fig. 3A). Once active transcription is entrenched, domain boundaries arise from the polymerase acting as a barrier in the ideal zone to prevent domain swelling due to its preferential function in this space.

To couple these processes into testable predictions of PD structure-function, we developed a mathematical model of these processes. This model pairs the mass-fractal physical properties of domains in their life cycle with the reaction processes above (see the Supplementary Material model for derivations). Capturing the mass-fractal–like properties of domains is crucial, as these properties generate a functional "interface zone" that is absent in domain

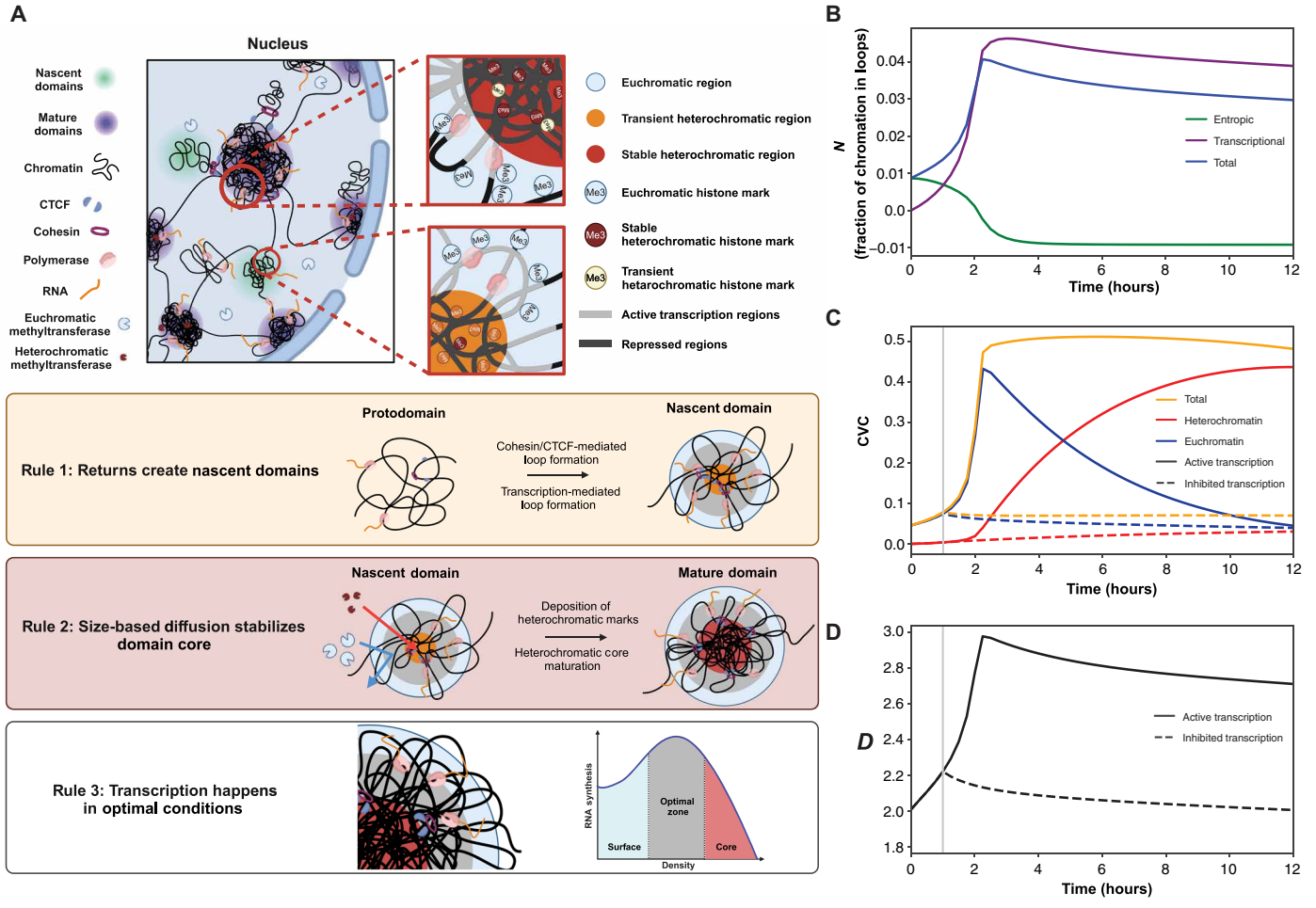

Fig. 3. A phenomenological model of domain self-assembly. (**A**) Visual schematic of domain structures within the nucleus demonstrating their intersection with RNA polymerase, cohesin, and nucleosome modifiers. Nascent domains and mature domains represent temporally evolving processes due to the intersection of nucleosome remodeling with return/loop-mediating processes. Proposed three-rule framework for domain assembly, stabilization, and function. Rule 1. The process of returns creates local density variations resulting in nascent domain formation. Rule 2. The excluded volume properties of domains and nucleosome remodeling enzymes result in preferential localization of heterochromatin remodeling enzymes to the interior of domains. Rule 3. Transcription depends nonmonotonically on local crowding and requires optimal zone configurations to accelerate. CTCF, CCCTC-binding factor. (**B**) Model predictions of the effect of transcriptional activation on the total number of observed loops (blue), entropic loops (green), and polymerase-mediated loops (purple) over time after transcriptional initiation. The negative frequency of entropic loops denotes the loss of entropically mediated loops over time as transcriptionally mediated loops and total loops increase. (**C**) Model predictions of the change in CVC overtime following initiation of transcriptional reactions at 1 hour with resulting accumulation of heterochromatin within the domain interior. Inhibition of transcription results in the converse phenotype with the decrease in density and loss of heterochromatin formation. (**D**) Consequence of transcriptional activity on polymer scaling, *D*, within domains after initiation at 1 hour demonstrating the maturation of domain structures with transcriptional activation (D 2.2 → 2.8).

models with solid or condensate structures. In condensate models, the interface is a negligible portion of the structure, reducing its functional capacity. In contrast, the mass-fractal structure on ChromSTEM allows for a large interface area where reactions can occur (Fig. 1).

One can reasonably start with a relaxed segment of chromatin in a confined nucleus without nucleosome modifications as this may reflect a sufficiently large segment of chromatin as the cell exits mitosis. Nascent domains could be formed by three processes capable of generating forced returns: transient contacts from spatial confinement, loop extrusion, and transcriptionally mediated contacts. This specifically occurs as these three processes produce a small pocket of local density, the size of which depends on the strength of the process (e.g., many P-P interactions in a short distance would produce a larger number nucleosome-nucleosome juxtaposition). The local density distribution produced creates a gradient for enzyme penetration that depends on their size and the excluded volume produced within this region. If this local density gradient is sufficiently high, then it results in preferential positioning of heterochromatin enzymes toward the interior and euchromatin enzymes near the outer zone and in the interdomain regions. Gene transcription reactions represent the most interesting case, since these reactions are nonmonotonically dependent on local density (peak efficiency, ~0.2 to 0.35) (*29*, *47*, *53*, *54*). As a result, transcription can both create domains and benefit from their formation from the resulting creation of an ideal functional "interface" zone in mature PDs.

One can visualize the model in the context of transcription as follows. Considering a genomic segment of ~100 kbp containing coding and noncoding regions spread out over a 100-nm^3 volume. Inefficient transcription reactions (P-P and E-P) and stochastic contacts create a pocket of increased local density consistent with a nascent domain (Fig. 3, A and B). If transcription remains ongoing, then the density further increases within this pocket producing physical gradient of positions for heterochromatin and euchromatin enzymes due to their sizes (Fig. 3A). With respect to the polymeric assembly, the model predicts that domains will transition from a weakly assembled nascent domain (D ~ 2.2) to a stable-state domain (D ~ 2.8; Fig. 3, A to C). In conjunction with domain maturation, transcriptional loops stabilize and persist at the domain periphery (Fig. 3, A to D) with a resulting decrease in entropic loops.

The net integration of these processes is domain self-assembly with a mass-fractal geometry. Transcription initiates the conditions to create a domain, nucleosome-modifying enzymes mature the domains, and transcription benefits from the created optimal zone while preventing further expansion. In the case of inhibition of RNA transcription, two processes are predicted to occur from the nonmonotonic dependence of transcription on local density. (i) A loss of nascent domains (Fig. 3, B to D) and (ii) unconstrained mature domain expansion as heterochromatin enzymes would proceed uninhibited outward. Reciprocally, active RNA polymerase has an optimal density for molecular activity, and from the model, we predict that the loss of heterochromatin cores could impair transcriptional activity by the loss of its ideal physiochemical conditions (Fig. 3A). As such, even where a gene is accessible, the lack of optimal conditions impairs transcription. This integration provides the basis for understanding the mechanistic role of chromatin PDs, their formation, and function. Instead of heterochromatin and euchromatin being dichotomous partitions, in domain geometry, they are an integrated physical and functional unit. Last, this integration provides the mechanistic explanation of the paradoxically inhibition of transcription with inhibition of heterochromatin enzymes that is tested within the manuscript.

Transcriptional inhibition and RAD21 depletion result in the loss of nascent domains

We next set out to test the predictions of this model at the level of nascent domain formation. As transcription and RAD21 loop extrusion produce long-range forced returns and interactions, the model predicts that transcriptional inhibition or RAD21 depletion results in primarily the loss of nascent domains. However, in contrast to RAD21, transcription would uniquely also act as a barrier element to prevent domain swelling by acting continuously along the intermediate zone of mature domains. To test this hypothesis, we used an RNA polymerase II (Pol II) auxin-inducible degron-2 (AID2) and a RAD21 AID2 cell line and performed Hi-C on cells with the depletion of these long-range regulators (*58*, *59*). As expected, the frequency of loops decreased at sites where loops were initially found (Fig. 4, A and B). To ensure the complete disruption of transcription, we then used actinomycin D (ActD) to inhibit the activity of all polymerases within the nucleus (*60*). On Hi-C with 4-μm ActD treatment, we again observed a decrease in loop frequency with transcriptional inhibition at the wild-type loci (Fig. 4C). Both RNA polymerase II depletion and ActD treatment result in an increase in entropic loops as observed in the formation of weak loop foci and the loss of native loops (Fig. 4, B and C, and fig. S2). To test the effect of this depletion on domain structure in situ, we analyzed the change in domains observed using ChromSTEM tomography on cells treated with 4-μm ActD and on depletion of RAD21. Consistent with the predictions from our model, ActD treatment and RAD21 depletion both result in the loss of nascent domains, with a pronounced 69% decrease in nascent domains (Fig. 4, D and E, and movies S2 and S3) upon ActD treatment.

Likewise, as predicted from transcription also acting as a barrier element to stabilize domains expansion, we observed the swelling of a subset of domains into very large structures (Fig. 4D) with low packing efficiency (60% increase) that was not observed on RAD21 depletion. To test whether these predictions in domain organization extended into live cells, we performed live-cell partial wave spectroscopic (PWS) microscopy to measure chromatin-average packing scaling D_n and the fractional moving mass (FMM) of chromatin under these conditions (*29*, *61*, *62*). While ChromSTEM measures the mass-fractal structure in individual domains, D_n measured by PWS microscopy is an ensemble average property of domains within a given chromatin region containing multiple domains and proportional to the D of individual domains and their volume fraction within the chromatin region. As long-range tethering would produce small clutches of nucleosomes moving as a paired functional element, a decrease in FMM would be consistent with impaired nascent domain assembly. Consistent with the findings on ChromSTEM tomography, we observe a decrease in D_n and FMM on ActD treatment consistent with the loss of domains and impaired formation of nascent domains. Furthermore, ActD treatment on PWS microscopy results in a much larger decrease in D_n and FMM compared to RAD21 depletion from the loss of both nascent and mature domain structures resulting in an increase in decaying domains upon transcriptional inhibition (Fig. 4, F and G). Notably, mature PDs were maintained upon RAD21 depletion, and decaying domains

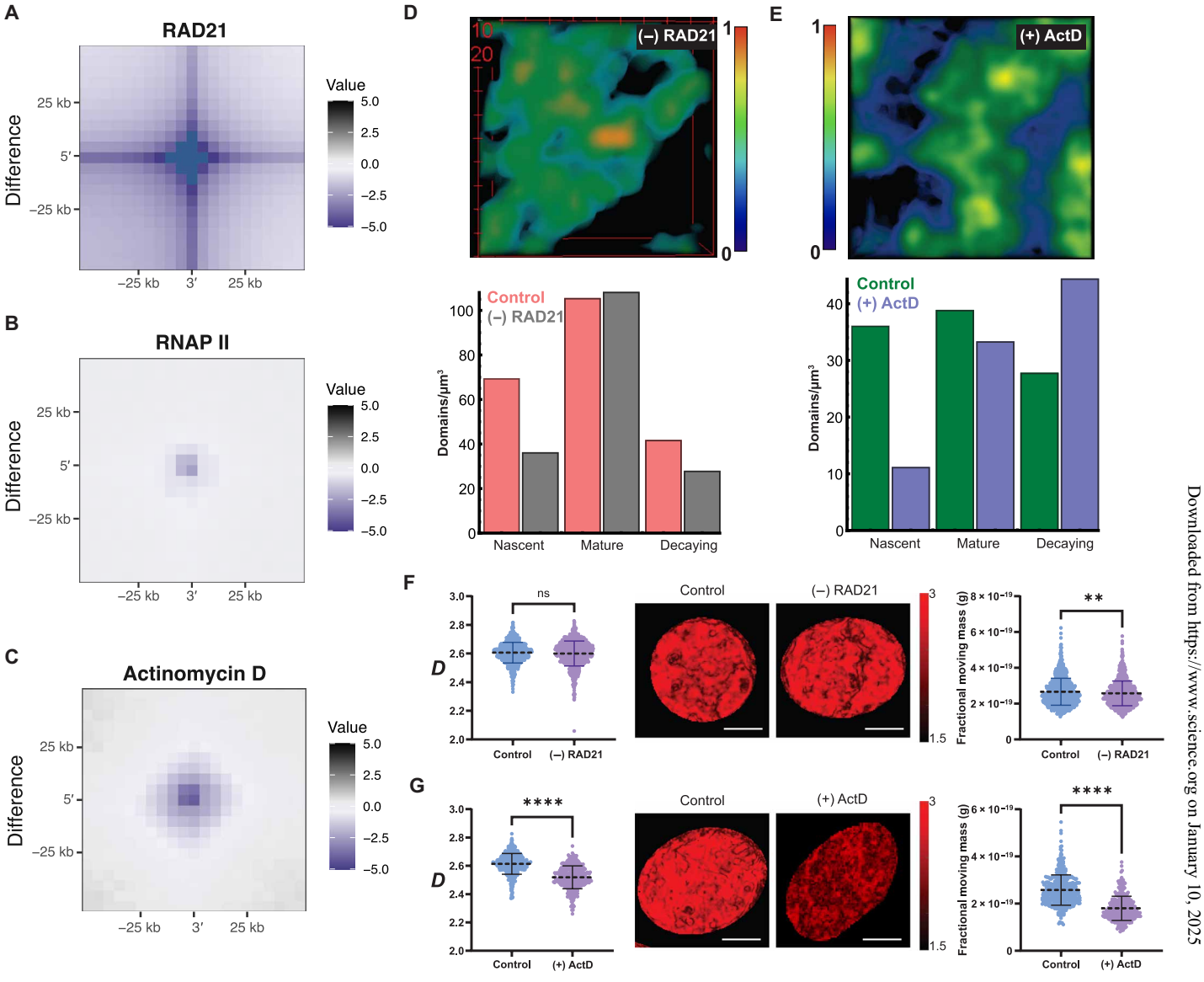

Fig. 4. Nascent domains are formed from transcriptionally mediate or cohesin-generated returns. (**A** to **C**) Analysis of native loop domains upon depletion of RAD21 (A), depletion of RNA polymerase II (B), and transcription inhibition with 4-μm ActD (C) demonstrating the loss of loop anchors with these perturbations. RAD21 and Pol-II depletion was achieved by 5-Ph-IAA treatment over 6 hours. (**D** and **E**) Representative PDs (200 nm by 200 nm) from RAD21-depleted cells (D) and 4-μm ActD-treated cells (E) showing porous structure and high-density cores are maintained in mature domains. Cross-sectional analysis of domains by size and packing efficiency demonstrates a disproportionate loss of low efficiency, small domains with inhibition of transcription and RAD21 depletion. (**F**) Live-cell PWS nanoscopy in RAD21-depleted HCT-116 cells at 4 hours demonstrating no impact on average chromatin scaling, *D*, and a decrease in fractional moving mass (FMM), consistent with impaired domain formation but retention of overall higher-order structure. (**G**) Live-cell PWS nanoscopy of ActD-treated BJ fibroblast cells demonstrating a decrease in *D* and a decrease in FMM consistent with the increase in decaying domains (large, low packing efficiency) and impaired domain formation. ns, not significant. $^{**}P < 0.01$, $^{****}P < 0.0001$.

increased with ActD treatment, which were features not observed on Hi-C at the level of change in TADs in either condition.

Consequently, this indicated that PDs are not merely a physical manifestation of TADs but represented an alternative regulatory framework in individual cells (fig. S2F). This finding is consistent with prior work with SIM, showing that chromatin nanodomains defined by DNA staining and nucleosome modifications were found to be sub-TAD structures that were unaltered by the depletion of RAD21 (*24*, *26*). Because of the resolution limit of SIM (80 to 100 nm), the challenge of converting the observed SIM signal intensity directly into mass density, and the challenge of mapping SIM images into polymeric folding, it would be difficult to probe the life cycle of domains observed on ChromSTEM exclusively with this modality (*24*, *26*).

Nucleosome modifications and transcription regulate domain stability

As evidenced from the model and ChromSTEM tomography, the observed PDs may align with the various structures observed using SIM and SMLM if heterochromatin is observed to spatially associate with active RNA polymerase and euchromatin

modifications as a unified, folding geometric structure described above (*24*, *26*, *28*, *34*, *63*, *64*). For these structures to be related, the distance at which polymerase and euchromatin marks occur at the boundary markers of a well-formed (presumably constitutive) heterochromatin core due to this region corresponds to the optimal densities (~3 to 5× the area of the dense interior) for the euchromatic and transcriptional enzymatic complexes (Fig. 1G and fig. S3). Although optimal transcriptional efficiency occurs for polymerases associated with dense domains, transcription must still occur (albeit less efficiently) in areas not associated with mature domains; otherwise, nascent domain formation would be rare. As such, it would be expected that a proportion of active RNA Pol-II is decoupled from constitutive heterochromatin and associates either with facultative heterochromatin or protodomains (Figs. 1 to 3). While not explored within this work, this consideration of the distribution of domain sizes, densities, and polymerase activity could have functional consequences depending on more complex cell states (e.g., differentiation, senescence, stem cells, and dormancy); each of which could have an associated polymerase-to-domain landscape. To test this hypothesis of frequent but not exclusive colocalization, we performed two- and three-color SMLM of serine-2 phosphorylation of Pol-II (Pol-II Ps2; associated with elongation) (*65*), with H3K27 acetylation (euchromatin) and H3K9me3 (constitutive heterochromatin) (Fig. 5A). To test whether heterochromatin cores and active Pol-II are codependent, we (i) inhibited EZH2 (GSK343; Fig. 5B) (*66*) to disrupt nascent domain maturation (H3K27me3); (ii) inhibited histone deacetylases (HDACs) with trichostatin A (TSA) (*57*) to disrupt existing mature heterochromatin domains (Fig. 5C); and (iii) disrupted transcription with ActD (Fig. 5D).

From the model, it is predicted that H3K27me3 depletion would result in the partial loss of H3K9me3 cores indirectly due to the disruption of domain maturation process, with the primary decrease in active Pol-II Ps2 loci occurring outside of H3K9me3 domains (a prediction that contrasts with a model of domains as continuously transitioning in density from H3K4me3 to H3K27me3 surrounding H3K9me3) (*24*). HDAC inhibition, with the direct disruption of mature domains, would produce several features: (i) The depletion of H3K9me3 would result in the loss of H3K27ac and Pol-II Ps2 predominantly within the low-density nuclear interior; (ii) there will be a greater loss in RNA polymerase loci in comparison to EZH2 inhibition due to the loss of optimal transcriptional domains; and (iii) the remaining Pol-II Ps2 would be mainly decoupled from H3K9me3. In strong agreement with our model, these specific predictions were observed (Fig. 5, E to G), including the previously unexplainable central elimination of both H3K27ac and H3K9me3 associated with TSA treatment on microscopy (Fig. 5, C, E, and F, and fig. S4). ActD-mediated transcriptional inhibition resulted in an overall decrease in the domain number with swelling of the remaining H3K9me3 domains as observed on ChromSTEM (Fig. 4) and also resulted in decoupling between active Pol-II and heterochromatin domains (Fig. 5, D to G) consistent with RNA polymerase facilitating domain assembly and acting as a barrier element to prevent domain expansion. Extended further to live-cell nanoscopy, the inhibition of transcription, the impairment of domain formation from EZH2 inhibition with GSK343, and the disruption of mature domains with histone deacetylase inhibition via TSA all result in loss of domains as evidenced by a decrease in D_n and the impaired ability for domain formation as measured by a decreased FMM (fig. S5).

Consistent with the findings on ChromSTEM and in our model, we found both the dissolution of constitutive H3K9me3 and the decoupling of Pol-II Ps2 from these structures (Fig. 5, A to G) with the inhibition of heterochromatin and transcription. If this spatial coupling extended into population data of loci for specific genes, then we hypothesized that similar features would be observed on ChIP-seq analysis by investigating the distal behavior of these features in 1D. With its role as a scaffold for nascent domain maturation, we predicted that H3K27me3 levels would correlate with the level of transcription on a long-range basis (e.g., on a per-chromosome analysis), whereas H3K9me3 would primarily couple with polymerase locally. As such, at the kilobase pair–to–megabase pair range, the model predicts that as RNA polymerase II density increases, the distance to H3K9me3 will decrease because of the increased efficiency of packing from transcriptional reactions. H3K27me3 will in contrast grow further away from genes with increasing level of Pol-II due to the transformation of domains from immature to mature structures. Using publicly available ChIP-seq data of H3K27me3, H3K9me3, and initiated polymerase (Pol-II Ps5) available through The Encyclopedia of DNA Elements (ENCODE) (*67*–*69*), these predictions hold with a correlation between H3K27me3 and polymerase coverage per chromosome (Fig. 5H). Likewise, as the density of Pol-II Ps2 per gene increases, the distance to the nearest H3K9me3 decreases monotonically (Fig. 5I) from ~100 to ~60 kbp on average (*65*).

Divalent ions are necessary for domain stabilization

Given the large accumulation of charged polyphosphates within the limited space of the domain interior, we hypothesized that counterions, especially multivalent ions such as magnesium and calcium, would be crucial to maintain domain integrity and nuclear size. In particular, the efficient conversion of nascent domains into mature structures will depend on the local density of DNA (and therefore nuclear volume) and, as a result, will require substantial charge neutralization to produce domain stability. Consequently, the loss of divalent counterions could prevent domain maturation and swell mature domains resulting in a loss in the total number of mature domains with increased size of remaining heterochromatic cores while also abating optimal conditions for transcription. On SMLM, this would be consistent with the decrease in the total number of H3K9me3 cores, an increase in the size of the remaining structures, and a decrease in the Pol-II Ps2 density surrounding the remaining domains. To test this hypothesis, we performed targeted chelation of intracellular divalent cations (Ca^{2+} and Mg^{2+}) with 1,2-bis(2-aminophenoxy)ethane-*N*,*N*,N′,N′-tetraacetic acid tetrakis(acetoxymethyl ester) (BAPTA-AM) and performed multicolor SMLM. On confocal microscopy, nuclear volume increases as expected from chelation of divalent ions (Fig. 6A). Consistent with the hypothesis that domains depend on ionic regulation, we observed that the number of domains decreased upon chelation (Fig. 6, B and F), with an increased size of the H3K9me3 clusters remaining and a decreased density of Pol-II Ps2 surrounding each cluster (Fig. 6, B to E). To directly investigate the influence of divalent cations on chromatin organization in living cells, we measured chromatin conformation from the level of PDs using PWS microscopy. Consistent with the results on SMLM upon BAPTA chelation, we observed a decrease in nuclear D_n and FMM, indicating a loss in mature domains and the process of their formation due to divalent cation chelation (Fig. 6F) comparable in magnitude to the effects of TSA-mediated HDAC inhibition (fig. S5).

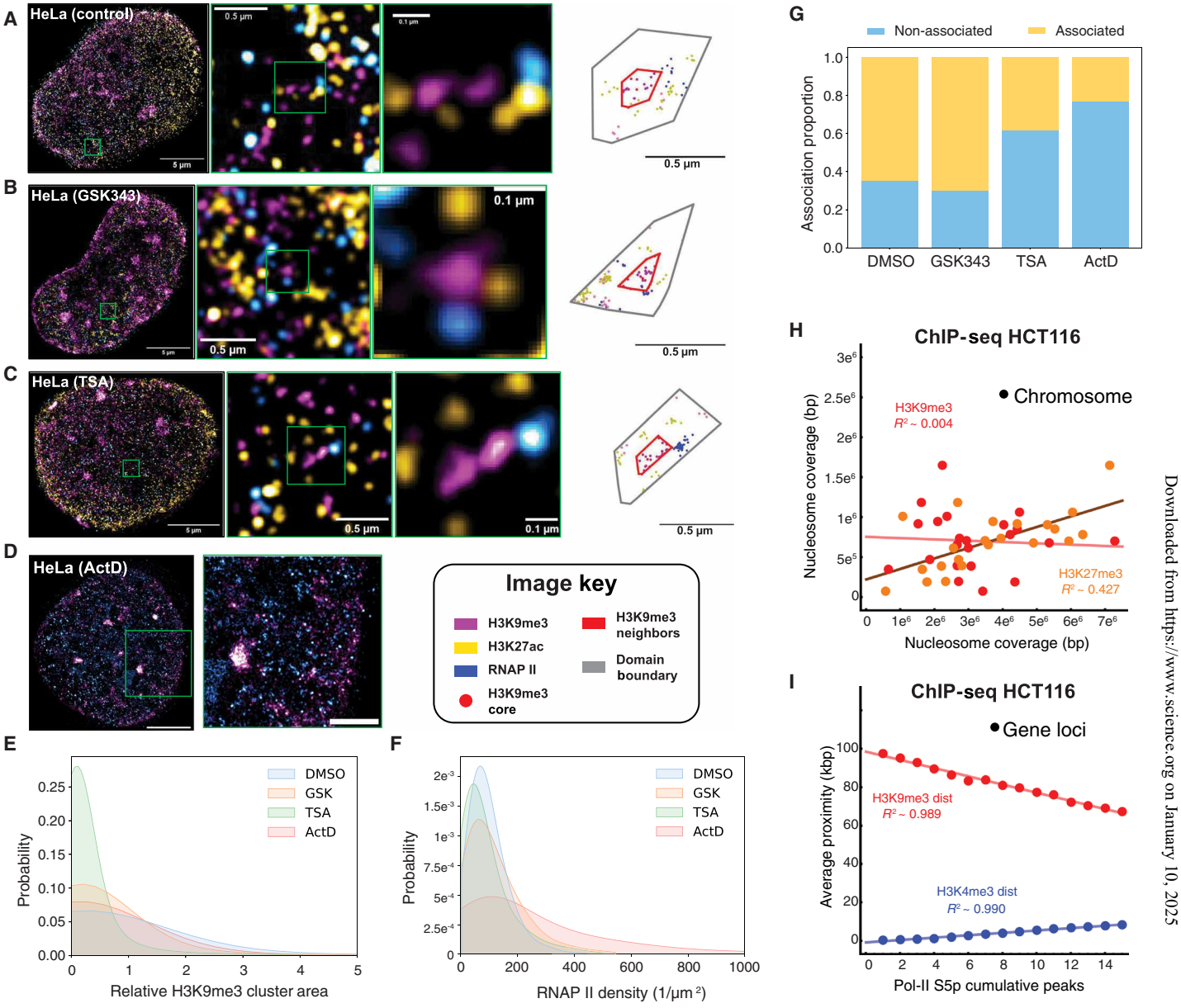

Fig. 5. Domains spatially couple heterochromatin, euchromatin, and active RNA polymerase. (**A**) Multiplex SMLM demonstrating the spatial localization of heterochromatin (H3K9me3, magenta), euchromatin (H3k27ac, yellow), and active RNA polymerase II [serine-2 phosphorylated (Pol2-PS2), blue]. This shows the complex spatial organization of chromatin into unified domain structures with heterochromatin cores (red) supporting Pol2-PS2 within an ideal functional zone (gray). (**B** to **D**) Multiplexed SMLM demonstrating the impact of inhibition of EZH2 (GSK343), HDACs (TSA), and transcription (ActD) on domain structure. Although mature domain structures remain, the disruption of transcription results in loss of H3K9me3 cores and their dissociation from active RNA polymerase. TSA-mediated HDAC inhibition results in a loss of heterochromatin and euchromatin marks with the most pronounced decrease observed in the nuclear interior. (**E**) Quantification of H3K9me3 core size upon HDAC inhibition, EZH2 inhibition, and transcriptional inhibition demonstrating a decrease in core size in all conditions imaged in HeLa cells above. (**F**) Quantification of Pol2-PS2 distribution upon HDAC inhibition, EZH2 inhibition, and transcriptional inhibition demonstrating a decrease in total Pol2-PS2 upon disruption of heterochromatin formation in HeLa cells above. (**G**) Quantification of the frequency of Pol2-PS2 observed near a surrounding H3K9me3 core in the above conditions. At the baseline, ~60% of Pol2-PS2 in HeLa cells is spatially associated with domains, and this is lost both with HDAC inhibition and disruption of transcription by ActD. (**H**) Analysis from ChIP-seq of the correlation between chromosome wide (a global measure) of heterochromatin markers with Pol2 serine-5 phosphorylated (Pol2-Ps5) isoform (initiated transcription). (**I**) Linear proximity analysis of constitutive heterochromatin (H3K9me3) and euchromatin (H3K4me3) as a function of Pol2-Ps5 density on gene bodies. Findings are consistent with H3K27me3 associating with nascent domains and H3K9me3 with mature domains. In contrast, H3K4me3 distance increases as a function of Pol2-Ps5 density likely due to localization in the outer zone.

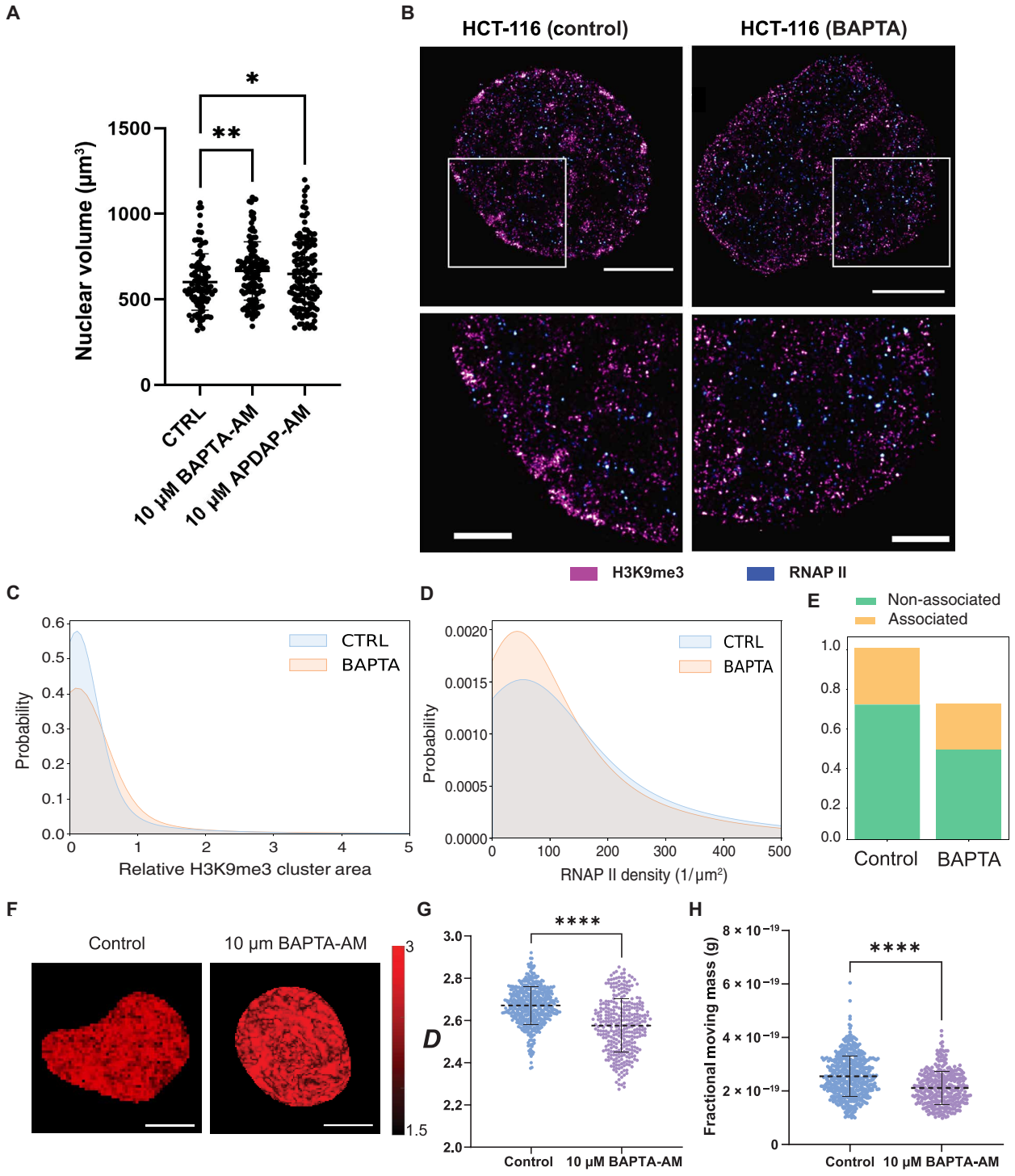

Fig. 6. Divalent ion chelation results in domain collapse. (**A**) Nuclear volume increases with chelation via BAPTA (calcium) and APDAP (magnesium) within 1 hour. (**B**) Representative multiplexed SMLM with Pol2-PS2 (blue) and H3K9me3 (magenta) in HCT-116 cells with and without chelation of divalent ions (calcium and magnesium) via BAPTA treatment at 1 hour. (**C**) Quantification of divalent chelation on H3K9me3 domains demonstrating a global loss of domain interiors. (**D** and **E**) Quantification of Pol2-PS2 demonstrating an increase in dissociation upon chelation. (**F** to **H**) Live-cell PWS nanoscopy of BAPTA-treated HCT-116 cells at 1 hour demonstrating a decrease in *D* (G) and a decrease in FMM (H) consistent with domain collapse and inhibition of domain formation. *$P < 0.05$, **$P < 0.01$, and ****$P < 0.0001$.

Inhibition of heterochromatin can suppress transcription in situ

From the model and the experimental results so far, an unexpected prediction is that heterochromatin formation is essential for proper transcription to occur (Figs. 3 to 5). Furthermore, the efficiency of heterochromatin formation will depend on nuclear CVC due to the effect volume has on enzyme distributions; therefore, decreased heterochromatin enzymatic activity or an increase in nuclear volume could result in a paradoxical global transcriptional decrease. This process arises from the nonmonotonic dependence of RNA polymerase on local crowding conditions in addition to its dependence on molecular features such as the dissociation constant for specific loci, transcription factor (TF) concentrations, and TF sequence binding affinities (*29*, *47*, *53*). Consequently, an overly accessible genomic segment without optimal physical conditions would be expected to have inefficient RNA synthesis. To test this prediction, we used HCT-116 cells, whose average CVC was observed to be ~0.2, and inhibited EZH2 with GSK343 and HDAC with TSA as above. Given the initial CVC, these perturbations would be expected to paradoxically disrupt transcription globally. Using two-color SMLM pairing the H3K9me3 structure with nascent RNA synthesis via 5-ethynyl uridine (EU) staining (*63*) in HCT-116 cells for 1 hour, we measured the resulting change in RNA synthesis with heterochromatin disruption. In dimethyl sulfoxide (DMSO) control HCT-116 nuclei, there is the visually apparent association between nascent RNA and H3K9me3, with a distribution of events observed both near the nuclear periphery and further into the interior (Fig. 7, A and B). With GSK343-mediated inhibition of EZH2, a notable loss of EU signal is observed visually (Fig. 7, C and D) within the non-nucleolar chromatin. As with EZH2-mediated inhibition, TSA treatment produces a marked decrease in the concentration of EU clusters (Fig. 7, E and F). On spatial analysis, we observed within the non-nucleolar interior that mRNA synthesis over an hour burst produces ~7.5 clusters/μm^2 (Fig. 7G). Quantitatively, we observed a decrease in EU foci to two clusters/μm^2 with GSK343 treatment, representing a 60%, and a drop in EU concentration to one cluster/μm^2 in the non-nucleolar chromatin, representing an ~80% decrease across the whole nucleus with TSA treatment. Near the nuclear border, we observed an initial lower rate of RNA synthesis as expected but a similar decrease in the total amount of RNA synthesis across GSK343 and TSA treatment (Fig. 7H). In the context of similar studies demonstrating a paradoxical dependence of RNA synthesis on the HDAC function, these results indicates how the disruption of domain geometry can result in the inhibition of gene transcription even as accessibility increases throughout the nucleus (*17*–*19*).

H3K9me3 domain cores form in noncoding regions of terminal myogenic genes during differentiation and depend on nuclear volume

Since CVC and heterochromatin are codependent in facilitating RNA synthesis from the perspective of chromatin domains, we hypothesized that aging-associated nuclear swelling (*70*, *71*) with the resulting loss in heterochromatin (*70*, *72*, *73*) could be associated with the transformation in chromatin PDs from the disruption of the self-assembly process. As such, the increased accessibility of the genome in aging can, in addition to the derepression of stem genes and promotion of increased DNA damage, also result in anergic transcription of necessary genomic locations. At the other end of the developmental spectrum, it is thought that heterochromatin accumulation represses inappropriate lineage genes to facilitate terminal differentiation (*74*). A model of these extremes is myogenesis and sarcopenia in aging. Clinically, understanding the regulation of muscle homeostasis has broad implications in human disease as sarcopenia is an independent prognostic marker of all-cause mortality and associated with impaired quality of life (*75*–*77*). Likewise, myogenic differentiation is a universal transcriptional network applicable to all vertebrate animals, with distinct roles of myogenic regulatory factors in the induction of stem cells into myoblasts and terminal differentiation as myotubes and muscle fibers (*78*, *79*). With these considerations in mind, we investigated myogenic differentiation and nuclear-associated swelling in sarcopenia as applicable testbeds for the predictive power of the model relevant to development and aging. As we have demonstrated so far, heterochromatin formation within PDs ensures proper domain geometry for transcription to occur on the periphery of mature domains. Consequently, the formation of H3K9me3 in noncoding segments would be hypothesized to associate with transcriptional activation by the self-assembly process. In terminal muscle differentiation, myogenin (Myog) is a crucial transcription factor regulating the transition from immature myoblasts into myotubes with its targeted deletion in mice resulting in complete loss of mature skeletal muscle (*80*, *81*). Key targets of Myog are the myosin heavy-chain genes, which are the primary structural component of skeletal muscle for appropriate mechanical contractility. As such, for terminal differentiation of myoblasts to myotubes to occur, Myog and myosin heavy-chain genes are up-regulated. From the three physical rules of the model: (i) Long-range interactions (e.g., a loop) should be evident before differentiation, (ii) H3K9me3 will accumulate adjacent within a noncoding region, and (iii) transcription amplifies in the formed domain with ideal configurations.

To test this hypothesis, we used publicly available ChIP-seq data through the ENCODE consortium (*67*–*69*) of H3K9me3, H3K27me3, H3K4me3, and gene expression and paired it with Hi-C of myoblasts and myotubes to examine the process of domain maturation. As expected from our model, a visually apparent chromatin loop domain dissipates, and H3K9me3 accumulates adjacent to Myog (Fig. 8, A to C) from the transition from myoblasts into myotubes. With respect to the myosin heavy-chain loci, we again observed the depletion of an adjacent chromatin loop (Fig. 8D) with the accumulation of H3K9me3 in noncoding regions adjacent to myosin heavy chains 1, 2, 4, and 8 (Fig. 8E and figs. S6 and S7). We predominantly observed accumulation adjacent to the fast-twitch myosin heavy chains (1 and 2) that are associated with the adult skeletal muscle function (Fig. 8F and fig. S7).

Naturally, sarcopenia would present the inverse of this process at these loci if disruption in chromatin PDs occurs from aging in muscle cells. To model this process, we considered the effect of nuclear swelling and its result on domain structure from the considerations we presented above. In contrast to topological features such as TADs and A/B compartments, PDs are affected by nuclear swelling due to rules two and three (*45*). We focused on myosin heavy chain 1 (Myh1) as its translated product decreases in aged muscle and therefore may represent sarcopenic transformation (*82*). Using SR-EV, we generated configurations of chromosome 17 with a fixed probability of long-range returns ($\alpha = 1.15$) and investigated the effect of decreased CVC from 0.2 to 0.08 on the structure of the domain cores at Myh1 (Fig. 8. G to I, and movie S4). By calculating the coordination number (CN) from SR-EV, we could estimate the likelihood of

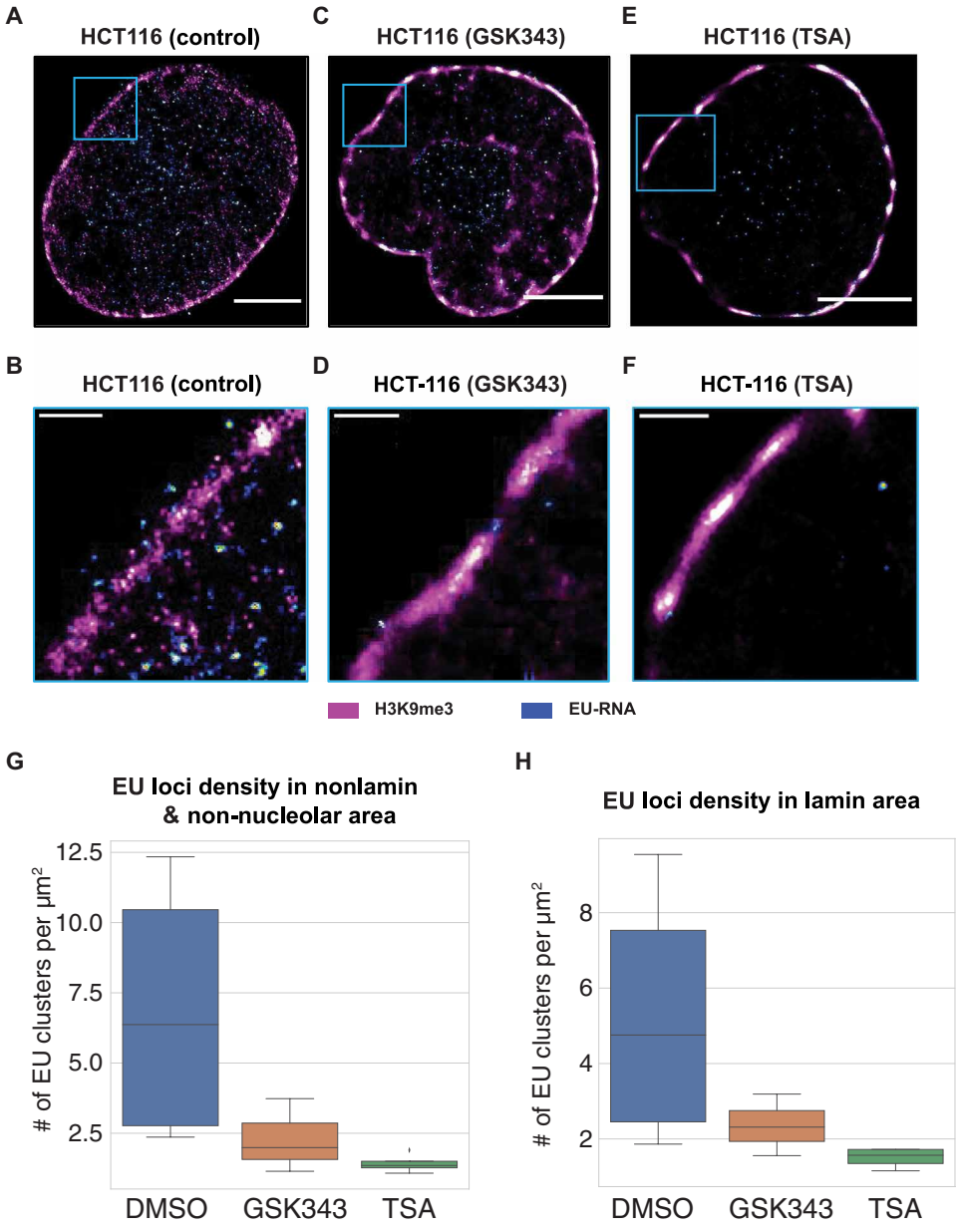

Fig. 7. Inhibition of heterochromatin enzymes paradoxically suppresses transcription in situ due to impairment of ideal conditions. (**A** to **F**) Representative multiplexed SMLM of nascent RNA measured by EU synthesis (blue) and H3K9me3 (magenta) in HCT-116 in controls compared to inhibition of EZH2 (B) and HDACs (C) demonstrating the profound loss of synthesis with inhibition of heterochromatin enzymes. (**G** and **H**) Quantification of the effect of heterochromatin enzyme suppression on RNA synthesis throughout the nucleus in comparison to adjacent to the nuclear border demonstrating loss of transcription independent of the nuclear region in HCT-116 cells. Note that the average CVC in HCT-116 cells is ~0.2 to 0.35 on ChromSTEM above, indicating that these cells are near optimal physiochemical conditions at the baseline. HDAC inhibition and EZH2 inhibition can still increase local transcription for initially high-density regions and globally in cell lines with a higher initial CVC (>0.35).

a gene segment being within a high-density region (CN > 8), an ideal region (6 to 7), and an outer zone region (CN < 5). Directly from the change in volume, we observe a decrease in the localization of exon elements from ideal conditions (contact with ~6 nucleosomes) toward accessible but less ideal configuration (contact with ~4 to 5 nucleosomes) as nuclear volume increased (Fig. 8H). Unexpectedly and consistent with the model, we found that the exon segments of Myh1 with a CVC of 0.16 generated with SR-EV were, on average, localized to ideal transcriptional conditions (Fig. 8I). Consequently, domain assembly is both observed at gene locations crucial for muscle differentiation, and the transformation of domains could occur from a process such as aging-associated nuclear swelling. In sum, these findings were consistent with a crucial role for domain assembly and maturation, with their degradation providing an additional deleterious consequence of pathological nuclear swelling.

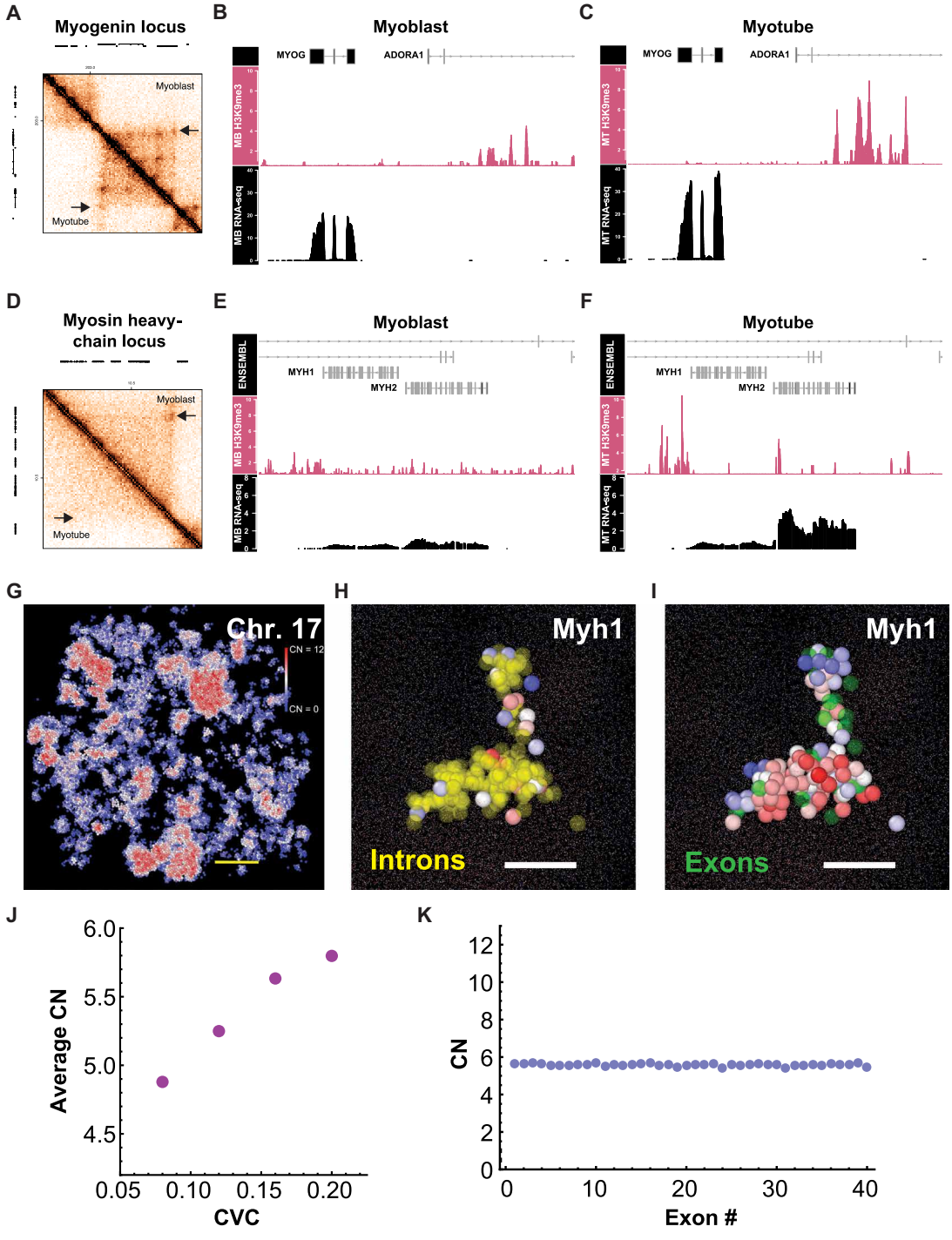

Fig. 8. Domain assembly occurs during myogenic differentiation and depends on CVC. (**A** to **C**) Transformation of the myogenic regulator, Myog, chromatin loci during development demonstrating the loss of loops (rule 1) with accompanying increase in heterochromatin adjacent to the gene body (rule 2) and acceleration of transcription (rule 3). (**D** to **F**) Transformation of the fast-twitch myosin heavy chains (Myh 1 and Myh2) chromatin loci during myoblast differentiation with loss of adjacent loop (rule 1) with accompanying increase in heterochromatin adjacent to the gene body (rule 2) and amplified transcription (rule 3) of structural myogenic proteins. (**G**) Representative configuration from SR-EV of chromosome 17 (scale bar, 200 nm) with color coding representing the coordination number (CN) representing the number of nucleosomes in contact. A CN of less than 5 represents an outer zone density configuration, 6 to 7 optimal transcriptional configuration, and greater than 7 representing an interior configuration. (**H**) Generated configuration from SR-EV of Myh1 representing quantified CN of exon segments with introns color coded in yellow (scale bar, 40 nm). Exon segments are frequently in the outer zone or ideal configurations. (**I**) Configuration from (H) with quantified CN of intron segments with exons color coded in green (scale bar, 40 nm). Inverse to exons, intronic elements are frequently found in domain interior configurations. (**J**) Average CN as a function of CVC with lower densities shifting toward outer zone configurations. (**K**) Average CN of Myh1 exons per nucleosome as a function of the exon segment at a CVC of 0.16 consistent with localization of coding elements into ideal transcriptional densities depending highly on CVC. RNA-seq, RNA sequencing; MB, myoblasts; MT, myotubes.

DISCUSSION

In this work, we investigate the structure of chromatin PDs identified on ChromSTEM tomography (Fig. 1) and their function in regulating gene transcription (Figs. 2 to 4). PDs are heterogeneous, conformationally defined assemblies whose function is tightly integrated with their mass-fractal geometry (Figs. 1F and 4, D to G). These domains exist across a conformational life cycle—nascent (poorly packed, small) domains form during transcription and loop extrusion, mature (efficiently packed) domains provide an ideal physical scaffold for transcription, and lastly, these domains collapse into decaying structures (large, poorly packed). This progression bidirectionally links a chromatin structure with gene regulation, as each stage of the life cycle reflects functional shifts in transcriptional activity (Figs. 3, 4, and 8).

Our modeling and simulations, coupled with experimental observations from ChromSTEM, multicolor SMLM, and PWS nanoscopy, indicate that nanoscopic chromatin organizations observed by other groups, including nucleosome clutches and heterochromatin domains/nanodomains, are part of the described domain-forming system (*24*, *26*, *28*, *33*, *34*, *63*). These collective findings demonstrate that connectivity does not necessarily translate into 3D space-filling conformations. Chromatin topology, as an ensemble property of a large number of cells, is not congruent to chromatin conformation. PDs are not simply the physical manifestation of TADs. Unlike TADs, which arise in measurements of connectivity, PDs undergo continuous structural transformations, driven by transcription and chromatin remodeling (Fig. 4). As we show, cohesin functions through generation of loop connections, creating nascent domains. Mature domains persist after RAD21 depletion, indicating that the regulatory function of mature domains is then independent of loop extrusion, including from ionic conditions and heterochromatin enzymes (Figs. 5 to 7). In addition, the formation of nascent domains is separately driven by transcription itself, and disruptions in domain maturation inhibit mRNA synthesis, illustrating the essential role of chromatin packing in transcription (Figs. 2, 3, and 8).

The interplay between transcription, heterochromatin remodeling enzymes, ion concentrations, and nuclear density suggests a complex regulatory system that bidirectionally integrates gene expression with chromatin organization. It is these properties that indicate PDs and transcription are coupled as an emergence phenomenon: The intersection of the three rules creates a complex regulatory, self-evolving structure. First, our findings demonstrate that PDs are self-assembling structures, forming through conformationally defined processes. Second, transcription critically depends on the deposition of heterochromatin in noncoding regions to maximize the efficiency of gene expression (Fig. 3). Last, this model explains why disruptions in heterochromatin, as seen in nuclear swelling during muscle aging (*72*, *82*), result in impaired cell function (Fig. 8). Insufficient nuclear density for domain maturation leads to the loss of heterochromatin, compromising transcription and potentially contributing to decreased transcriptional synthesis as nuclei swell in aging.

This domain life cycle model challenges the traditional framework of chromatin regulation (*5*, *6*, *8*–*11*, *37*, *38*, *83*). The simplistic view that dense chromatin (heterochromatin) suppresses gene expression while loose chromatin (euchromatin) facilitates it fails to capture the complexity observed at the nanoscale. Traditional models evolved from low-resolution techniques like wide-field microscopy and confocal microscopy, which could not identify the finer nanoscopic features of chromatin within the nucleus. Instead, they identified high-density (heterochromatin) and low-density (euchromatin) regions at the micron-scale (*6*, *8*). These models influenced correlative interpretations of Hi-C connectivity (A and B compartments) and ChIP-seq segmentation (hetero- and euchromatin) (*6*, *7*). However, these approaches lacked the necessary nanoscale information on conformationally defined chromatin PD life cycle that only became available through the advent of ChromEM (*25*). Our findings, rooted in the mass-fractal geometry of PDs, demonstrate that chromatin regulation involves continuous transitions between dense cores, intermediate zones (active polymerases), and low-density outer zones, forming a unified, dynamic structure. If chromatin were governed solely by self-attractions (A to A and B to B), then one would likely observe discrete, functionally independent condensates (*9*, *10*). Instead, this model offers a more cohesive explanation of chromatin behavior, integrating transcriptional regulation with structural dynamics.

Last, one can consider the implications of these findings to the concepts of transcriptional memory and the manipulation of cell behavior. Features of the PD life cycle echo reinforcement learning in computational networks (*84*). A transcriptional stimulus forms a nascent domain, and sustained signaling (positive reinforcement) with the right physical context matures the structure. This indicates that sustained, strong transcriptional signals will become physically encoded into the physical organization of a PD (Fig. 3). Once matured, this domain becomes a fixed physical object akin to a "transcriptional memory," predisposing or preventing alternative configurations that would need the genomic segments allocated to the formed domain in future responses. Encoding transcriptional memory in 3D chromatin domains solves several critical problems: The analog nature of domains as a source of information and multiple degrees of freedom afforded by the processes that regulate the rate of domain formation for a given level of nascent domain-generating transcriptional activity (e.g., nuclear ionic environment, crowding, and availability of histone modifying enzymes) may increase the flexibility of the system. It allows for long-term memory through domain stabilization while retaining the possibility of reprogramming through domain degradation; and the reinforcement learning properties of the system may facilitate, if necessary, cells' continuous responding to changing stressors and stimuli. However, the 3D nature of the information encoding presents a new problem: A 3D structure per se cannot be propagated through cell division. Epigenetic histone modifications may help solve this problem. Although epigenetic modifications as a mechanism to pass transcriptional information through cell division is well established, the prevailing context has centered around epigenetic modifications as the primary and original source of transcriptional information. The results presented in this work may point out to a possibility of another complementary origin of epigenetic information that may originate from the primary process of chromatin domain formation (new memory = new domains), which subsequently guides the deposition of histone marks. In this context, epigenetic marks can be thought of as projecting the information encoded by 3D chromatin domains into the 1D epigenetically marked DNA sequence. In turn, since epigenetic marks can be heritable through mitosis, the marks may carry with them information about the genomic locations of chromatin domains into daughter cells, thus creating a long-term transcriptional memory, repeating the cycle and solving the problem of the heritance of 3D chromatin domains as elements of transcriptional memory. Paired with information on the location of a

mature domain core, tools that allow the deposition of heterochromatin could potentially accelerate the activation of one or several genes.

This addresses a conundrum of epigenetic regulation of transcription that most epigenetic regulators are gene sequence agnostic, and still, epigenetic modifications may result in reproducible and specific transcriptional outcomes. A part of the answer might be in conformationally defined chromatin domains. Through excluded volume effects, chromatin domains might be able to add gene specificity to otherwise nonspecific epigenetic regulators, as, for instance, they would be expected to act differently inside domain cores versus transcriptionally active ideal zones. In other words, these results suggest a hypothesis that chromatin conformation into domains induces geometric specificity instead of segment specificity to create a regulatory scheme independent of sequence. It might be instructive to distinguish the two types of epigenomic memory, one stored by histone and DNA modifications versus transcriptional memory, which arises in part but not solely due to epigenetic modifications. This work raises questions of the deleterious consequences of a malformed transcriptional memory. It is possible that a sustained signal in the wrong context could produce physically encoded programs resulting in pathological cellular states. Moreover, it highlights the potential for sequential stimuli [e.g., tumor necrosis factor (TNF) followed by interleukin-12 (IL-12) exposure] to generate different transcriptional outcomes compared to concurrent stimuli (TNF + IL-12 together). By removing or inserting domain cores before these processes, it is worth considering if transcriptional memory could be manipulated in different disease contexts. These insights could inform the understanding of disease processes, such as chronic inflammation or cancer, where improper domain maturation locks cells into deleterious transcriptional states (*85*, *86*).

MATERIALS AND METHODS

Cell culture

HCT-116 cells [American Type Culture Collection (ATCC), #CCL-247] and U2OS cells (ATCC, #HTB-96) were grown in McCoy's 5A modified medium (#16600-082, Thermo Fisher Scientific, Waltham, MA). HeLa cells (ATCC, #CCL-2) were cultured in RPMI 1640 medium (#11875127, Thermo Fisher Scientific, Waltham, MA). BJ CRL-2522 fibroblasts (BJ) cells were cultured in minimum essential media (#11095080, Thermo Fisher Scientific, Waltham, MA). All cell culture media were supplemented with 10% fetal bovine serum (#16000-044, Thermo Fisher Scientific, Waltham, MA) and penicillin-streptomycin (100 μg/ml; #15140-122, Thermo Fisher Scientific, Waltham, MA). All cells were maintained under recommended conditions at 37°C and 5% CO_2. Cells were allowed at least 24 hours to readhere and recover from trypsin-induced detachment. All imaging was performed when the surface confluence of the dish was between 40 and 70%. All cells in this study were maintained between passages 5 and 20. All cells have been tested for mycoplasma contamination (ATCC, #30-1012K) before starting experiments, and they have given negative results.

Drug treatments

AID2 cell lines

HCT-116 RAD21-mAID-Clover CMV-OsTIR1(F74G) cells (*58*, *59*) were plated at 50,000 cells per well of a six-well plate (Cellvis, P12-1.5H-N). To induce rapid and efficient depletion of mAID-fused proteins (RAD21), 5-Ph-IAA (#HY-134653, MedChemExpress), 5-(3,4-dimethylphenyl)-indole-3-acetic acid, 5-(3-methylphenyl)-indole-3-acetic acid, and 5-(3-chlorophenyl)-indole-3-acetic acid were dissolved in DMSO to make a 500 mM stock solution and further diluted with DMSO to working stock solution of 1 mM immediately before the experiment. A final concentration of 1 μM 5-Ph-IAA was added to HCT-116 RAD21-mAID-Clover CMV-OsTIR1(F74G) cells for 6 hours.

Inhibition of transcription

HCT-116 and BJ cells were plated at 50,000 cells either per well of a six-well plate (Cellvis, P12-1.5H-N). For inhibition of RNA synthesis, ActD (*60*) (#11805017, Gibco) was dissolved in DMSO to make an 8 mM stock solution and further diluted with cell media to make a working solution of 80 μM immediately before the experiment. A final concentration of 4 μM was added to HCT-116 and BJ cells for 1 hour to completely arrest all polymerases.

Inhibition of EZH2 and HDACs

For EZH2 inhibition, GSK343 (#1346704-33-3, Millipore Sigma) was dissolved in DMSO to make a 10 mM stock solution and added to U2OS cells at a final concentration of 10 μM for 24 hours. For HDAC class 1 and 2 inhibition, TSA (*3*, *18*) (#58880-19-6, Millipore Sigma) was added to HCT-116 cells at a final concentration of 300 nM for 24 hours.

Chelation of divalent cations

For ionic inhibition, membrane-permeable BAPTA-AM (*87*) (#B6769, Invitrogen) was dissolved in DMSO to make a 10 mM stock solution and added to HCT-116 cells at a final concentration of 10 uM for 1 hour to chelate calcium and magnesium ions.

Live-cell PWS microscopy acquisition and analysis

For live-cell measurements, cells were imaged and maintained under physiological conditions (5% CO_2 and 37°C) using a stage-top incubator (Stage Top Systems; In Vivo Scientific, Salem, SC). The PWS optical instrument was built on a commercial inverted microscope (DM IRB; Leica, Buffalo Grove, IL) supplemented with a Hamamatsu Image electron multiplying (EM) charge-coupled device camera C9100-13 coupled to a liquid crystal tunable filter (Cambridge Research and Instrumentation, Inc., Woburn, MA) for hyperspectral imaging. Spectrally resolved images of live cells were collected between 500 and 700 nm with a 2-nm step size. Broadband illumination was provided by an Xcite-120 light-emitting diode lamp (Excelitas, Waltham, MA). The spectral SD (Σ) of the interference scattering originating from chromatin is calculated from the captured images. Variations in the refractive index distribution, Σ, can be evaluated by the mass density autocorrelation function to calculate chromatin packing, scaling *D*. (*29*, *36*, *62*)

Nuclear volume quantification

For nuclear volume quantification, HCT-116 cells were treated with ion chelators [BAPTA-AM; acetoxymethyl ester (APDAP-AM)] for 60 min, fixed in 4% paraformaldehyde for 10 min, and then stained with 4′,6-diamidino-2-phenylindole. Fluorescence images were captured using an Olympus IX-71 inverted microscope with a high-efficiency electron-multiplying charge-coupled device (EMCCD) camera (Olympus, Tokyo, Japan). The images were then analyzed using FIJI software. The nucleus was identified using binary masks, then the 3D Object Counter plugin segmented the images, the regions of interest (ROIs) were added to 3D Manager, and lastly the

ROIs were applied to the original z-stack image to determine the volume and intensity of each nucleus.

Chromatin electron microscopy

ChromEM staining and sample resin preparation

Cells are first washed with Hanks' balanced salt solution, without calcium and magnesium prewarmed to 37°C. The cells are then fixed with a fixative solution prepared with 2% paraformaldehyde, 2.5% glutaraldehyde, and 2 mM calcium chloride prepared in 0.1 M sodium cacodylate buffer at a pH of 7.4, for 30 min at room temperature and another 30 min at 4°C. Cells are then washed in 0.1 M sodium cacodylate buffer and then placed in a blocking buffer prepared with 10 mM glycine, 10 mM potassium cyanide, and 0.1 M sodium cacodylate buffer for 15 min.

Nuclear DNA staining is then carried out by staining with 10 μM DRAQ5 (Thermo Fisher Scientific) in 0.1% saponin and 0.1 M sodium cacodylate buffer for 10 min and covered and on ice; then, it was washed three times with blocking buffer for 5 min each, followed by submerging in 2.5 mM 3,3-diaminobenzidine tetra hydrochloride [Electron Microscopy Sciences (EMS)]. Photooxidation of DAB was conducted under epifluorescence with a cyanine5 (Cy5) filter for 5 min with a 100× oil objective. After photobleaching, cells are again washed five times for 2 min each. Cells are then stained with heavy metal to enhance the DNA density of DAB polymer precipitates using 2% osmium tetroxide prepared with 2 mM calcium chloride, 0.15 M sodium cacodylate buffer, and 1.5% potassium ferrocyanide, for 30 min. After heavy metal staining, cells were washed five times for 2 min each with Millipore water.

Samples are then gradually dehydrated and embedded into Durcupan epoxy resin following the standard procedures as previously described in (*25*, *29*, *36*). The resin-embedded samples were then processed for ultramicrotomy using an ultramicrotome (UC7, Leica) and a 35° Diatome knife, cutting the resin sample block into 120-nm sections, and laid onto slot grids with the carbon/Formvar film (EMS). The samples are then coated with gold nanoparticles as fiducial markers on both surfaces.

ChromSTEM imaging and reconstruction

The Hitachi 2300 STEM was used to collect high-angle annular dark-field (HAADF) images throughout a dual tilt series collection at every 2° increments from −60° to 60°. IMOD was used to align the images, and reconstruction was done using the Tomopy penalized maximum likelihood algorithm. IMOD was then used to combine the tomograms from two individual tilt axes.

After reconstruction, the voxel values were capped to the top and the bottom 0.1% values to remove outliers. The values were then normalized between 0 and 1 for analysis.

Chromatin domain analysis

Chromatin domains were identified and analyzed following the approach published previously (*29*, *36*). Domain centers were selected as local maxima with prominence of >1.5× SD of pixel values on a 2D projected chromatin map of the tomogram after a Gaussian filter with a 5-pixel radius followed by contrast limited Adaptive Histogram Equalization (CLAHE) contrast enhancement.

An 11 × 11–pixel window is then used to select the center pixel in each domain. The total intensity of chromatin is measured as a function of distance away from the center pixel. The power-law scaling region is identified by MATLAB "ischange" function on log mass versus log radius. The domain size is determined at the point where the power-law scaling is deviated from the fitting by 5% difference or when the local exponent D reaches 3. For the calculation of packing efficiency A, the elementary chain size R_{min} is determined by a 10% difference from the power-law scaling at the lower end of the power-law scaling region, and A is calculated by $A = CVC/[(R_{domain}/R_{min})^{(D-3)}]$, where I is the average intensity of the domain, R is the radius of the domain, and D is the power-law exponent.

High-throughput chromatin conformation capture

Sample preparation

Cultured cells were treated with 1 μM 5-PH-IAA (MedChemExpress, HY-134653) for 6 hours or with DMSO at an equivalent concentration for 6 hours (*58*, *59*). At 6 hours, cells were harvested at 1.2×10^6 cells per sample and transferred to a 50-ml Falcon tube, where they were centrifuged for 10 min at 450*g* at room temperature. The supernatant was removed, and cells were resuspended in 20 ml of cold fresh media. At this point, 540 μl of 37% formaldehyde was added to bring the final concentration to 1% formaldehyde and fix the cells for 10 min. Upon fixation, the reaction was quenched with 10 ml of 3 M tris (pH 7.5) for 15 min. Cells were then centrifuged for 10 min at 800*g* and 4°C. After resuspension at the desired concentration, individual samples were snap-frozen in liquid N_2.

Hi-C library generation

To wash the nuclei, samples were thawed and resuspended in 50 μl of ice-cold phosphate buffer, followed by the addition of 150 μl of ice-cold ribonuclease (RNase)–free water. Fifty microliters of buffer C1 (Qiagen EpiTect Hi-C Kit) was added to each sample and mixed. Samples were then centrifuged at 2500*g* and 4°C for 5 min. The supernatant was aspirated, and the nuclear pellet was resuspended in 500 μl of RNase-free water, before being centrifuged again at 2500*g* and 4°C for 5 min. Library generation and subsequent steps used proprietary reagents from the Qiagen's EpiTect Hi-C Kit (Qiagen, 59971). Washed nuclei were digested with according to the EpiTect Hi-C protocol using a proprietary enzyme cocktail that cut at the GATC motif. Nuclei were end-labeled with biotin followed by ligation for 2 hours at 16°C. Ligated chromatin was then decross-linked using 20 μl of proteinase K solution at 56°C for 30 min and then 80°C for 90 min. Ligated, decross-linked DNA was purified using a Qiagen column kit (Qiagen, 59971) and resuspended in 130 μl of elution buffer.

Library fragmentation

Hi-C library samples were fragmented to a median size of between 400 and 600 bp using a Covaris E220 sonicator with a sample size of 130 μl and the settings in table S4. Samples were purified for fragments between 400 and 500 bp using a Qiagen bead purification size exclusion kit (Qiagen, 59971).

Hi-C sequencing library generation

Hi-C samples were streptavidin-purified to enrich for properly ligated contact pairs using streptavidin beads and a magnetic bead rack. Beads were first washed in 100 μl of bead wash buffer, resuspended in 50 μl of bead resuspension buffer, and then mixed with 50 μl of Hi-C sample. The mixture was then incubated at room temperature for 15 min in a thermal mixer at 1000 rpm. Enriched bead-bound DNA was then end-repaired, phosphorylated, and poly-adenylation (poly-A)–tailed using a combined ER/A-tailing solution. The samples were incubated for 15 min at 20°C followed by incubation at 65°C for 15 min. Beads were then washed once with 100 μl of bead wash buffer, washed again with 95 μl of adapter ligation buffer, and resuspended in adapter ligation buffer in preparation for

ligation of Illumina adapter sequences. Each sample was mixed with 5 μl of one of six Illumina adapter sequences (specified in the Qiagen protocol appendix) and 2 μl of ultralow input ligase. These samples were then incubated for 45 min. Following adapter ligation, each sample was washed three times before adding 400 μl of library amplification mixture to the beads. Samples were then distributed equally across eight wells of a 96-well polymerase chain reaction (PCR) plate and cycled using the following parameters on an Eppendorf Mastercycler X50s thermocycler (table S5).

Following sequencing, PCR reactions for each sample were pooled and cleaned using a Qiagen QIAseq library purification kit (Qiagen, 59971). Library quality was assessed using a High Sensitivity DNA Assay on an Agilent Bioanalyzer 2100 and a Qubit dsDNA High Sensitivity Assay. Libraries were quantified using a KAPA ROX Low Master Mix qPCR library quantification kit on a QuantStudio 7 Flex instrument. Two samples per lane were sequenced on an Illumina NovaSeq 6000, generating between 400 and 600 million 150-bp paired-end reads per sample.

Hi-C data processing and analysis

ActD-treated samples and 5-ph-IAA–treated samples were aligned to hg38 using Borrow-Wheeler Aligner version 0.7.17 and processed using the SLURM version of Juicer version 1.6 (https://github.com/aidenlab/juicer) (*88*) on the Quest High-Performance Computing Cluster provided by Northwestern University. Processing included in the Juicer pipeline included removal of duplicates, exclusion of improperly ligated fragments, and mapping of Hi-C contacts with the GATC motif. Statistics generated for each replicate can be found in the Supplementary Materials. Individual replicates were checked for reproducibility using standard heuristics and combined as a mega map using Juicer's Mega script to increase sample resolution. TAD identification was generated using Juicer's Arrowhead (https://github.com/aidenlab/juicer/wiki/Arrowhead) (*88*). Loops were identified using Juicer's HiCCUPS (https://github.com/aidenlab/juicer/wiki/HiCCUPS) (*88*). Compartment eigenvector analysis and Pearson correlation analysis were generated using Juicer's Eigenvector and Pearsons scripts, respectively, or using built-in functions in GENOVA (*89*). Aggregate TAD Analysis and Aggregate Peak Analysis were generated using GENOVA (https://github.com/robinweide/GENOVA). Contacts were dumped using Hi-C Straw (https://github.com/aidenlab/straw) and used for downstream analysis. Visualization was also done using GENOVA. All other analyses were custom-generated in R. All codes used in this publication are available on Github at github.com/BackmanLab.

Myoblast and myotube samples were aligned to hg38 and processed using the Next Flow Core Hi-C pipeline (https://github.com/nf-core/hic/tree/2.1.0). Coolers (*90*) were generated at 5- and 80-kb resolutions from the Hi-C Pro output. Contacts were dumped using cooltools (https://github.com/open2c/cooltools) (*91*) and used for downstream analysis. Contact maps were visualized using GENOVA.

Single-molecule localization microscopy

Multicolor SMLM sample preparation

Primary antibodies rabbit anti-H3K9me3 (Abcam), mouse anti-H3K27ac (Thermo Fisher Scientific), rat anti-RNA polymerase II (Abcam), and mouse anti-H3K27me3 (Abcam) were aliquoted and stored at −20°C. Secondary antibodies goat anti-rabbit AF647 (Thermo Fisher Scientific), goat anti-rabbit AF568 (Thermo Fisher Scientific), and goat anti-rat AF488 (Thermo Fisher Scientific) were stored at 4°C.

Three-label SMLM sample preparation is done via three sequential staining processed for the three respective targets.

1) Cells were plated on no. 1 borosilicate bottom eight-well Lab-Tek Chambered cover glass at a seeding density of 12.5k. After 48 hours, the cells underwent fixation for 10 min at room temperature with a fixation buffer composed of 3% paraformaldehyde and 0.1% glutaraldehyde in phosphate-buffered saline (PBS). Samples were then washed in PBS for 5 min and then quenched with freshly prepared 0.1% sodium borohydride in PBS for 7 min. Two more wash steps were performed after quenching.

2) Permeabilization was done with blocking buffer composed of 3% bovine serum albumin (BSA) and 0.5% Triton X-100 in PBS for 1 hour, and then samples were immediately incubated with rabbit anti-H3K9me3 (Abcam) in blocking buffer for 1 to 2 hours at room temperature and a shaker. Samples were then washed three times with a washing buffer composed of 0.2% BSA and 0.1% Triton X-100 in PBS.

3) Samples were then incubated with the corresponding goat antibody–dye conjugates and anti-rabbit AF647 (Thermo Fisher Scientific) for 40 to 60 min at room temperature on the shaker. After incubation, samples were washed two times in PBS for 5 min on a shaker, and then samples were either imaged for first labeled target or incubated overnight in a modified version of the aforementioned blocking buffer (10% goat serum + 90% prior composition).

4) After overnight blocking, the samples would then go through the same protocol as in step 3 (primary and secondary antibody incubation) but this time with modified blocking buffer (90% original blocking buffer + 10% goat serum) and washing buffer (99% original washing buffer + 1% goat serum) for both the second and third targets. The second target primary antibody is a rat anti-RNA polymerase II (Abcam), and the secondary antibody is goat anti-rat AF488 (Abcam). As described before, there is an overnight blocking step in between labels at 4°C. The third target primary antibody is a mouse anti-H3K27ac (Thermo Fisher Scientific), and the secondary antibody is goat anti-rat AF568 (Abcam). After primary and secondary incubation, the samples are washed three times with PBS and then stored at 4°C.

Single-molecule localization data analysis

Acquired data were first processed using the ThunderSTORM ImageJ (*92*) plugin to generate the reconstructed images for visualization via the average shifted histogram method, as well as the localization datasets. Each localization dataset was corrected for drift and subsequently filtered such that remaining data had an uncertainty of less than or equal to 40 nm. Localization coordinates (x and y) were then used in a Python point-cloud data analysis algorithm which used the scikit-learn DBSCAN method (parameter choice: 50-nm maximum distance between points and minimum of three points per cluster) to cluster the heterochromatic localizations. Cluster size was determined by the area of the convex hull fit of the clustered marks and then normalized relative to a circular cluster with radius of 80 nm. Sample (heterochromatin, euchromatin, and RNAP II) density was measured by counting the number of corresponding STORM markers in concentric rings from the identified cluster center, normalized by a ring area. RNAP II association was determined by measuring the number of RNAP II that fall within five times expansion of the area outside of the cluster relative to all RNAP II localizations. The outside cluster condition signifies RNAP II not within any analysis area and thus not associated with heterochromatic clusters. Data shown are for concatenation of $n \geq 4$ cell

replicates with approximately >500 heterochromatic clusters for each nucleus.

Utilization of artificial intelligence tools

Artificial intelligence (AI) tools were used within this manuscript as follows. Commands were given to ChatGPT 4.0 to assess the logic structure of written portions and redrafted if the wrong conclusions were identified from the provided passages. For example, the following prompt of "what is the author saying here" with paragraphs from that section. Final proof editing and revisions of the manuscript were performed by the authors. Furthermore, AI tools were not used for the direct writing of the manuscript. For assistance with visualization of data, ChatGPT 4.0 was prompted to generate code to produce plots as with the following commands. "i would like to make a barchart in mathematica with 4 pairs of data. The first value in each pair will be visualized in gray but i want to color the values in the second pair with black, purple, orange, and blue." The produced code was modified to include the relevant and to confirm the values produced. The visualization was likewise modified for clarity by the authors. Last, ChatGPT was used to help visualize the calculated R_g for visualization from the AlphaFold configurations as follows "can you use the pdb that I provided to calculate the radius of gyration of suv39h1? "Relevant libraries were then installed to facilitate the calculations. This was extended to other enzymes with the obtained PDBs from AlphaFold using additional prompts such as "i would like to calculate the radius of gyration of all the heterochromatin enzymes. Can we modify the pdb script to load all of the molecules above and produce their size in angstrom" and "can we modify this code to include the get_protein_name and output the name, size in kilodaltons, and radius of gyration." The mathematical operators produced for Python were verified. As the mass is known for each enzyme, the output mass was verified against another source such as genecards.org.

Analysis of enzyme size

AlphaFold (*50*) Protein Data Bank (PDB) structures of transcription factors and euchromatin and heterochromatin enzymes were obtained (table S1), and the radius of gyration R_g was calculated from the produced atomic structures as the square root of the mean distance from the center of mass. The respective R_g were 4.1, 5.5, and 3.0 nm on average for these proteins (table S6). Statistical testing was performed on heterochromatin compared to euchromatin enzymes based on the calculated R_g with a two-tailed, unpaired *t* test with a *P* value of 0.0005. No corrections for multiple comparisons were made as these were not performed. For RNA polymerases, PDB structures were obtained from the research collaboratory for structural bioinformatics (RCSB), and the R_g was calculated as above. As these polymerase structures were in complex with DNA, their mass compared to size was not included; however, their average R_g was ~5 nm, slightly below the size of transcription factors.

Modeling chromatin domains and molecular dynamic study of enzyme penetration

The stochastic returning excluded volume (SR-EV) configurations were obtained using the procedure described by Carignano *et al.* (*46*) using an overall volume fraction $\phi = 0.12$ and folding parameter $\alpha = 1.10$ for investigation of enzyme penetration. DNA sequences from reference sequence (RefSeq) were superimposed onto polymer simulations from SR-EV to analyze the structure at the myosin heavy chains as a function of density with ϕ ranging from 0.08 to 0.20 and a fixed folding parameter $\alpha = 1.15$. The CN was calculated as the number of nucleosomes in contact with the nucleosome of interest with values ranging from 0 (isolated nucleosome) to 12 (in contact with 12 neighbors) representing various degrees of compaction. To understand the accessibility of free proteins on different regions of chromatin as a function of local volume fraction, we performed molecular dynamic simulations of free spherical particles immersed in static SREV configurations where the nucleosomes were represented as oblate Gay-Berne objects (*93*). To eliminate boundary effects, we used SREV configurations created in a cubic box of 1300 nm in size and with periodic boundary conditions. Ten thousand spherical particles were randomly inserted in the system with no overlaps between them and with the model nucleosomes. We simulated four different sphere sizes, represented by a Lennard-Jones size parameter $\sigma = 3, 6, 9$ and 12 nm. The simulations were performed using the Large-scale Atomic/Molecular Massively Parallel Simulator (LAMMPS) (*94*) molecular dynamic software, under number volume temperature (NVT) conditions, using a reduce length unit $r_u = 10$ nm and a reduced temperature $T^* = 2.5$. The interaction parameters, described in the standard LAMMPS input notation, are the following:

```
units lj
atom_style ellipsoid
set type 1 shape 1.0 1.0 0.5  # Ellipsoids
set type 2 shape 0.3 0.3 0.3  # Spheres (in this case, 3 nm diameter)
#
# pair_style gayberne gamma upsilon mu cutoff
pair_style gayberne 1.0 1.0 1.0 3.0
#
# pair_coeff ty1 ty2 eps sig (eps_a eps_b eps_c)_i (eps_a eps_b eps_c)_j
pair_coeff 1 1 1.0 1.0  1.7 1.7 3.4  0.0 0.0 0.0
pair_coeff 1 2 1.0 1.0  1.7 1.7 3.4  0.0 0.0 0.0
pair_coeff 2 2 1.0 1.0  1.7 1.7 1.7  0.0 0.0 0.0
```

ChIP-seq analysis

Using data available through ENCODE (table S2) (*67*–*69*), we analyzed the relationship between serine-5 phosphorylated RNA polymerase (Pol-II PS5; initiation of transcription) (*65*) and epigenetic marks as follows. RefSeq gene positions were consolidated to a single, longest defined start/stop position of the reported isoforms of the same gene annotation. Following consolidation, the mean location of each peak for the different marks (table S2) was identified such that their *P* value was <0.1. Genes were then organized by the cumulative number of PolII-PS5 peaks within each gene from 1 to 15 in HCT-116 cells. The absolute linear distance from each PolII-PS5 to the nearest chromatin mark was then calculated. The cumulative density function of distances was used to identify the average distance as a function of the number of identified peaks with a linear regression fit to the resulting value as shown. With respect to the per-chromosome analysis, the total segment length of each mark was calculated, and marks were compared to the coverage of PolII-PS5 across the somatic chromosomes with the exclusion of X and Y chromosomes from this analysis due to their distinct mechanisms of heterochromatin formation.

Phenomenological loop domain formation model

We developed a computational model to describe three primary rules that regulate the polymeric structure-function of chromatin

domains: (i) Returns (loops) create local areas of high density from long-range confinement, (ii) nucleosome remodeling enzyme localization depends on their excluded volume interactions with polymeric domains, and (iii) transcriptional reactions nonmonotonically depend on local crowding conditions from the competition between enzyme diffusivity and the free-energy of the chemical reactions resulting in a zone of optimal efficiency (Fig. 3A). For simplicity, we describe transcription as the primary generator of returns. One could also include cohesin-mediated loop extrusion as a second process, but the consequence is like transcription alone.

We start by defining basic physical properties of a PD formed from polymeric folding of chromatin in nuclear space. We define ϕ as the chromatin volume fraction (CVC within the main text), the space occupied by chromatin in the theoretical volume. $\phi = 0$ denotes a volume free of chromatin, and $\phi = 1$ represents a fully filled volume occupied by the chromatin polymer. Since chromatin behaves as a power-law polymer at domain length scales, ϕ directly relates to folding properties that are infrequently used in the context of gene regulation. From prior work in ChromEMT, the smallest element of the chromatin polymer chain, r_{min}, is ~10 nm. The density of chromatin within a volume can then be described by from the relationship from r_{min} by the scaling exponent, D, and the efficiency with polymer fills this space A (the packing efficiency).

Rule 1

Within a domain volume, one can consider loops per unit volume as quantizable events ("loopons"), N, as a function of their spatial and genomic distance. In a relaxed polymer without returns or confinement, the likelihood of two segments of a polymer in contact decays exponentially as a function of the linear genomic separation, X, by the contact-scaling exponent, s. In the context of a crowded nucleus with enzymatically mediated but infrequent looping events, loop events arise stochastically from confinement or from transcription creating quantized events along a segment that decreases the distance. Contact scaling of the segments as a function of genomic distance depends on the frequency of loop events by $s \approx \ln\left(\frac{N_0}{N}\right) / \ln\left(\frac{X}{X_0}\right)$. From imaging experiments and polymer modeling, contact scaling relates to D by $s \sim 1/D$ [which has been described extensively by Li *et al.* (*29*)]. We consider a fractal random walk polymer approximate for which $s \sim 3/D$. Thus, it arises that the effect of loop frequencies in a nuclear volume are quantifiable by

$$D \cong 3 * \left[\log\left(\frac{X}{X_0}\right) \Big/ \log\left(\frac{N_0}{N_{Opt}}\right)\right] \quad (1)$$

where X_0 is the base genomic chain length and N_0 is the base loop volume fraction. It is reasonable to start with a distance ratio (X/X_0) of ~24 (gene length on average, ~24 kbp; chain length, ~1 kbp) and use $N_0 \sim 1$ to indicate that each base pair cannot be split between two separate loops. From this relationship, we can then calculate the N_{Opt}, the optimal loop capacity for a given set of conditions (for example, monomer-monomer and monomer-solvent interactions) within the volume.

The change in the domain D over time, $D(t)$, depends on the evolution of the total number of loops over time, $N(t)$, and their change over time as follows

$$\frac{dD(t)}{dt} = \frac{N'(t)}{N(t)} \times \frac{D(t)}{\log\left[N(t)/N_0\right]} \quad (2)$$

In principle, N can be positive or negative, as it quantizes loop behavior along a chain to describe loop formation and loss. The total N is the sum of the loop volume fraction from enzymatic processes (primarily transcription; N_t) and entropic events ($N_{\Delta s}$)

$$N = N_t + N_{\Delta s} \quad (3)$$

While N is generally positive, N_t and $N_{\Delta s}$ can be negative representing the elimination of previously formed loops. From the reasonable assumption that transcription can only occur when engaged in euchromatic segments, ϕ_e, active transcription results in the formation of returns that are actively removed via the family of topoisomerases (TOPs). Consequently, loops mediated by transcription evolve by

$$\frac{dN_t(t)}{dt} = \phi_e(t)\Gamma_{POL2} - N_t(t)\Gamma_{TOP} \quad (4)$$

Here, Γ_{POL2} denotes the rate of transcriptional mediated loop formation, and Γ_{TOP} is the rate at which topoisomerase degrade these loops.

We can similarly incorporate the formation and degradation of entropic loops through the interplay between optimal loop capacity N_{Opt} and the current loop occupancy N

$$\frac{dN_{\Delta s}}{dt} = \Gamma_{\Delta s} * \left[N_{Opt} - N(t)\right] \quad (5)$$

with $\Gamma_{\Delta s}$ being the rate of entropic loop formation and decay, which captures the process by which loops evolve independent of protein-mediated extrusions. From Eqs. 3 to 5, we can model the time evolution of loop formation, and Eqs. 1 and 2 model the formed domain structure.

Rule 2

Having described how N intersects with D in domains, we can use the relationship between D, ϕ, and A to describe the temporal evolution of the space-filling properties of domains. Chromatin is frequently described by the functional modifications into heterochromatin (poorly accessibly, ϕ_h) and euchromatin (highly accessible, ϕ_e). The total ϕ is therefore the sum of euchromatin and heterochromatin in the theoretical volume, $\phi = \phi_e + \phi_h$. Considering that CVC decreases with radial distance r from the center of a chromatin domain as $\left(r/r_{min}\right)^{D-3}$ and restricting the focus in time during the timescales of return formation through possible degradation, we quantify the temporal evolution of domains and their average volume fraction by

$$\phi(t) = \phi_e(t) + \phi_h(t) = \frac{3}{D(t)} \times A(t)\left(\frac{r_{min}}{r}\right)^{3-D(t)} \quad (6)$$

From Eq. 6, the temporal evolution of ϕ in relation to the polymeric folding of the chromatin in the limiting case of a perfectly space-filling, efficiently packed polymer $A = 1$ and $D = 3$ converges as expected to the value of 1 (fully compacted). Likewise, $\phi(t)$ will converge to $A(t)$ in the limiting case of $D = 3$ or to $3*A(t)/D(t)$ for $r = r_{min}$. From ChromEMT data (*25*), a heterochromatin chain is more tightly packed; therefore, A is proportionally related to the fraction of euchromatin and heterochromatin. We define A of a domain that is fully euchromatic as A_e and fully heterochromatic as A_h. Experimentally, we observe that domains exist with $A = 1$ and are therefore presumably fully heterochromatic chains result in $A_h = 1$.

We can then extrapolate A for intermediate fractions of euchromatin and heterochromatin as follows

$$A(t) = \left\{ \left[\phi_h\,(t) + A_e * \phi_e\,(t) \right] / \left[\phi_h\,(t) + \phi_e\,(t) \right] \right\} \tag{7}$$

where A_e is less than 1. Chromatin-modifying enzymes have a distinct distribution of sizes that correlates with their posttranslational modification of nucleosomes (Fig. 2B). From SR-EV simulations (Fig. 2, C and D), enzyme size results in a spatial preference for heterochromatin enzymes localizing within a domain interior, whereas larger euchromatin enzymes and transcription factors favor the periphery (Fig. 2, C and D).

To model this, we create a generalized reaction rate equation based on prior work studying the interactions of excluded volume with transcription reactions for each reactant group: RNA polymerase (Γ_{POL2}), topoisomerase (Γ_{TOP}), heterochromatic modifiers (Γ_h), and euchromatic modifiers (Γ_e). As an approximation, this can be captured by

$$\Gamma_x = \Gamma_x(t) = B_x * \phi * \left(1 - \frac{\phi}{\sigma_e}\right) \tag{8}$$

Equation 8 is then used to account for differences in activity based on the likelihood of localization of the enzyme and scaled relative to the size of Pol-II (*47*). This is modeled by the rate coefficients, B_x, to account for differences in protein activity as an initial approximation, as we expect that some proteins have different rates of activity based on their sizes in diffusion-limited reactions with smaller proteins have a greater B_x than larger ones. Naturally, there is a ϕ at which the protein can no longer diffuse or perform its function due to its size, which is denoted as σ_x. The values of B_x and σ_x that can then be used for each type of protein type for this model can be found in table S1 and depend on the findings from the SR-EV simulations in Fig. 2.

The change in the domain structure from these enzymatic processes is thus quantified by

$$\frac{d\phi_h(t)}{dt} - \frac{d\phi_e(t)}{dt} = \phi_e(t)\Gamma_h(t) - \phi_h(t)\Gamma_e(t) \tag{9}$$

which captures the change in domain density from the rate of compaction of euchromatin into heterochromatin via heterochromatin-modifying proteins (SUV39H1/2 or HDACs) and the rate of decompaction of heterochromatin into euchromatin.

Over time, domain core densities will exclude larger proteins and only allow the transit of small molecules or heterochromatin proteins. As a result, domain interiors become favorable for cross-linking reactions from small proteins such as HP1a. To model this process in relation to the rate of entropic relaxation, we assume that HP1a cross-linking is a function of local density by, ps, and counteracts the maximal entropic rate $B_{\Delta s}$

$$\Gamma_{\Delta s} = B_{\Delta s} * e^{\left(\frac{-\phi_h}{\phi * ps}\right)} \tag{10}$$

Even as domains have variations in their density radially, the probability distribution function of ϕ for these molecules in a domain is captured by

$$\langle \Gamma_x(r) \rangle = \int_{PD} \Gamma_x(\phi) \times \mathrm{pdf}(\phi) d\phi \tag{11}$$

Extending this into the probability distribution function in a power-law domain, we observe that the

$$\mathrm{pdf}(\phi) \propto \left(\frac{r_{min}}{r}\right)^{3-D} \times r^2 \tag{12}$$

For the purposes of simulations, this can be expanded into the following analytic form

$$\langle \Gamma_x \rangle = B_x * A * D * \left(\frac{r_{min}}{r}\right)^D * \left\{ \begin{array}{c} \left[\frac{1}{2D-3} * \left(\frac{r_{min}}{r}\right)^D - \frac{1}{3*(D-2)} * \frac{A}{\phi_c} * \left(\frac{r_{min}}{r}\right)^3\right] * \left[\left(\frac{r_{min}}{r}\right)^{3-3D}\right] + \\ \left[\frac{1}{3*(D-2)} - \frac{1}{2*(D-3)}\right] * \left(\frac{A}{\phi_c}\right)^{\left[3-2*D/(D-3)\right]} \end{array} \right\} \tag{13}$$

Rule 3

Excluded volume within the nucleus affects the transcription rate such that the resulting relationship of mRNA concentration as a function of ϕ has a nonmonotonic behavior with a peak centered around $\phi \sim 0.2$ to 0.35 depending on the binding efficiency of transcription reactants, the dissociation constants, and the efficiency of RNA polymerase synthesis. Crowding produces the observed nonmonotonic behavior from two competing processes: (i) Crowding without attractions slows molecule diffusion as a function of size and density; (ii) excluded volume facilitates stabilization of intermediary complexes by increasing the entropy of the system. We define this region of ideal density as the "goldilocks" zone, ϕ_{GL}

$$\phi_{GL} = A * \left(\frac{r_{GL}}{r_{min}}\right)^{D-3} \tag{14}$$

In turn, this can be converted to identify the radius where ideal conditions occur

$$r_{GL} = r_{min} * \left(\frac{\phi_{GL}}{A}\right)^{\left[1/(D-3)\right]} \tag{15}$$

Within the manuscript, the solved equations are as follows

$$N = N_t + N_{\Delta s} \tag{3}$$

$$\frac{dN_t(t)}{dt} = \phi_e(t)\Gamma_{POL2} - N_t(t)\Gamma_{TOP} \tag{4}$$

$$\frac{dN_{\Delta s}}{dt} = \Gamma_{\Delta s} * \left[N_{Opt} - N(t)\right] \tag{5}$$

$$\phi(t) = \phi_e(t) + \phi_h(t) = \frac{3}{D(t)} \times A(t) \left(\frac{r_{min}}{r}\right)^{3-D(t)} \tag{6}$$

$$\frac{d\phi_h(t)}{dt} - \frac{d\phi_e(t)}{dt} = \phi_e(t)\Gamma_h(t) - \phi_h(t)\Gamma_e(t) \tag{9}$$

$$\Gamma_{\Delta s} = B_{\Delta s} * e^{\left(\frac{-\phi_h}{\phi * ps}\right)} \tag{10}$$

and the following initial conditions are $D(0) = 2.01$, $N_t(0) = 0$, $N_{\Delta s}(0) = N_{Opt}$, and $\phi_h\ (0) = 0$ where N_{Opt} will depend on D. When solving for D_{pd}, N_t, $N_{\Delta s}$, ϕ_e, and ϕ_h, simulations were run until N reached a derivative of zero, indicating that the system had reached a steady state. Remaining parameters present within table S3.

Supplementary Materials

The PDF file includes:

Figs. S1 to S7
Tables S1 to S6
Legends for movies S1 to S4

Other Supplementary Material for this manuscript includes the following:

Movies S1 to S4

REFERENCES AND NOTES

1. Y. Shin, C. P. Brangwynne, Liquid phase condensation in cell physiology and disease. *Science* **357**, eaaf4382 (2017).
2. D. Husmann, O. Gozani, Histone lysine methyltransferases in biology and disease. *Nat. Struct. Mol. Biol.* **26**, 880–889 (2019).
3. J. I. Nakayama, T. Hayakawa, Physiological roles of class I HDAC complex and histone demethylase. *J. Biomed. Biotechnol.* **2011**, 129383 (2011).
4. C. Arnould, V. Rocher, F. Saur, A. S. Bader, F. Muzzopappa, S. Collins, E. Lesage, B. Le Bozec, N. Puget, T. Clouaire, T. Mangeat, R. Mourad, N. Ahituv, D. Noordermeer, F. Erdel, M. Bushell, A. Marnef, G. Legube, Chromatin compartmentalization regulates the response to DNA damage. *Nature* **623**, 183–192 (2023).
5. E. H. Finn, T. Misteli, Molecular basis and biological function of variability in spatial genome organization. *Science* **365**, eaaw9498 (2019).
6. E. Lieberman-Aiden, N. L. van Berkum, L. Williams, M. Imakaev, T. Ragoczy, A. Telling, I. Amit, B. R. Lajoie, P. J. Sabo, M. O. Dorschner, R. Sandstrom, B. Bernstein, M. A. Bender, M. Groudine, A. Gnirke, J. Stamatoyannopoulos, L. A. Mirny, E. S. Lander, J. Dekker, Comprehensive mapping of long-range interactions reveals folding principles of the human genome. *Science* **326**, 289–293 (2009).
7. S. S. P. Rao, M. H. Huntley, N. C. Durand, E. K. Stamenova, I. D. Bochkov, J. T. Robinson, A. L. Sanborn, I. Machol, A. D. Omer, E. S. Lander, E. L. Aiden, A 3D map of the human genome at kilobase resolution reveals principles of chromatin looping. *Cell* **159**, 1665–1680 (2014).
8. M. Falk, Y. Feodorova, N. Naumova, M. Imakaev, B. R. Lajoie, H. Leonhardt, B. Joffe, J. Dekker, G. Fudenberg, I. Solovei, L. A. Mirny, Heterochromatin drives compartmentalization of inverted and conventional nuclei. *Nature* **570**, 395–399 (2019).
9. K. Polovnikov, S. Belan, M. Imakaev, H. B. Brandão, L. A. Mirny, A fractal polymer with loops recapitulates key features of chromosome organization. bioRxiv 478588 [Preprint] (2022). https://doi.org/10.1101/2022.02.01.478588.
10. G. Fudenberg, M. Imakaev, C. Lu, A. Goloborodko, N. Abdennur, L. A. Mirny, Formation of chromosomal domains by loop extrusion. *Cell Rep.* **15**, 2038–2049 (2016).
11. J. Nuebler, G. Fudenberg, M. Imakaev, N. Abdennur, L. A. Mirny, Chromatin organization by an interplay of loop extrusion and compartmental segregation. *Proc. Natl. Acad. Sci. U.S.A.* **115**, E6697–E6706 (2018).
12. S. Fujishiro, M. Sasai, Generation of dynamic three-dimensional genome structure through phase separation of chromatin. *Proc. Natl. Acad. Sci. U.S.A.* **119**, e2109838119 (2022).
13. O. Adame-Arana, G. Bajpai, D. Lorber, T. Volk, S. Safran, Regulation of chromatin microphase separation by binding of protein complexes. *eLife* **12**, e82983 (2023).
14. G. Shi, D. Thirumalai, From Hi-C contact map to three-dimensional organization of interphase human chromosomes. *Phys. Rev. X* **11**, 011051 (2021).
15. Q. Szabo, F. Bantignies, G. Cavalli, Principles of genome folding into topologically associating domains. *Sci. Adv.* **5**, eaaw1668 (2019).
16. C. L. Woodcock, R. P. Ghosh, Chromatin higher-order structure and dynamics. *Cold Spring Harb. Perspect. Biol.* **2**, a000596 (2010).
17. I. M. Baker, J. P. Smalley, K. A. Sabat, J. T. Hodgkinson, S. M. Cowley, Comprehensive transcriptomic analysis of novel class I HDAC proteolysis targeting chimeras (PROTACs). *Biochemistry* **62**, 645–656 (2023).
18. C. B. Greer, Y. Tanaka, Y. J. Kim, P. Xie, M. Q. Zhang, I.-H. Park, T. H. Kim, Histone deacetylases positively regulate transcription through the elongation machinery. *Cell Rep.* **13**, 1444–1455 (2015).
19. O. M. Dovey, C. T. Foster, N. Conte, S. A. Edwards, J. M. Edwards, R. Singh, G. Vassiliou, A. Bradley, S. M. Cowley, Histone deacetylase 1 and 2 are essential for normal T-cell development and genomic stability in mice. *Blood* **121**, 1335–1344 (2013).
20. B. E. Bernstein, T. S. Mikkelsen, X. Xie, M. Kamal, D. J. Huebert, J. Cuff, B. Fry, A. Meissner, M. Wernig, K. Plath, R. Jaenisch, A. Wagschal, R. Feil, S. L. Schreiber, E. S. Lander, A bivalent chromatin structure marks key developmental genes in embryonic stem cells. *Cell* **125**, 315–326 (2006).
21. N. Liu, M. Fromm, Z. Avramova, H3K27me3 and H3K4me3 chromatin environment at super-induced dehydration stress memory genes of Arabidopsis thaliana. *Mol. Plant* **7**, 502–513 (2014).
22. Z. Wang, A. G. Chivu, L. A. Choate, E. J. Rice, D. C. Miller, T. Chu, S.-P. Chou, N. B. Kingsley, J. L. Petersen, C. J. Finno, R. R. Bellone, D. F. Antczak, J. T. Lis, C. G. Danko, Prediction of histone post-translational modification patterns based on nascent transcription data. *Nat. Genet.* **54**, 295–305 (2022).
23. S. S. P. Rao, S.-C. Huang, B. G. S. Hilaire, J. M. Engreitz, E. M. Perez, K.-R. Kieffer-Kwon, A. L. Sanborn, S. E. Johnstone, G. D. Bascom, I. D. Bochkov, X. Huang, M. S. Shamim, J. Shin, D. Turner, Z. Ye, A. D. Omer, J. T. Robinson, T. Schlick, B. E. Bernstein, R. Casellas, E. S. Lander, E. L. Aiden, Cohesin loss eliminates all loop domains. *Cell* **171**, 305–320.e24 (2017).
24. E. Miron, R. Oldenkamp, J. M. Brown, D. M. S. Pinto, C. S. Xu, A. R. Faria, H. A. Shaban, J. D. P. Rhodes, C. Innocent, S. de Ornellas, H. F. Hess, V. Buckle, L. Schermelleh, Chromatin arranges in chains of mesoscale domains with nanoscale functional topography independent of cohesin. *Sci. Adv.* **6**, eaba8811 (2020).
25. H. D. Ou, S. Phan, T. J. Deerinck, A. Thor, M. H. Ellisman, C. C. O'Shea, ChromEMT: Visualizing 3D chromatin structure and compaction in interphase and mitotic cells. *Science* **357**, eaag0025 (2017).
26. Q. Szabo, A. Donjon, I. Jerković, G. L. Papadopoulos, T. Cheutin, B. Bonev, E. P. Nora, B. G. Bruneau, F. Bantignies, G. Cavalli, Regulation of single-cell genome organization into TADs and chromatin nanodomains. *Nat. Genet.* **52**, 1151–1157 (2020).
27. J. M. Luppino, D. S. Park, S. C. Nguyen, Y. Lan, Z. Xu, R. Yunker, E. F. Joyce, Cohesin promotes stochastic domain intermingling to ensure proper regulation of boundary-proximal genes. *Nat. Genet.* **52**, 840–848 (2020).
28. M. V. Neguembor, L. Martin, Á. Castells-García, P. A. Gómez-García, C. Vicario, D. Carnevali, J. AlHaj Abed, A. Granados, R. Sebastian-Perez, F. Sottile, J. Solon, C.-T. Wu, M. Lakadamyali, M. P. Cosma, Transcription-mediated supercoiling regulates genome folding and loop formation. *Mol. Cell* **81**, 3065–3081.e12 (2021).
29. Y. Li, A. Eshein, R. K. A. Virk, A. Eid, W. Wu, J. Frederick, D. VanDerway, S. Gladstein, K. Huang, A. R. Shim, N. M. Anthony, G. M. Bauer, X. Zhou, V. Agrawal, E. M. Pujadas, S. Jain, G. Esteve, J. E. Chandler, T.-Q. Nguyen, R. Bleher, J. J. de Pablo, I. Szleifer, V. P. Dravid, L. M. Almassalha, V. Backman, Nanoscale chromatin imaging and analysis platform bridges 4D chromatin organization with molecular function. *Sci. Adv.* **7**, eabe4310 (2021).
30. B. Bintu, L. J. Mateo, J.-H. Su, N. A. Sinnott-Armstrong, M. Parker, S. Kinrot, K. Yamaya, A. N. Boettiger, X. Zhuang, Super-resolution chromatin tracing reveals domains and cooperative interactions in single cells. *Science* **362**, eaau1783 (2018).
31. A. N. Boettiger, B. Bintu, J. R. Moffitt, S. Wang, B. J. Beliveau, G. Fudenberg, M. Imakaev, L. A. Mirny, C. Wu, X. Zhuang, Super-resolution imaging reveals distinct chromatin folding for different epigenetic states. *Nature* **529**, 418–422 (2016).
32. A. Hafner, M. Park, S. E. Berger, S. E. Murphy, E. P. Nora, A. N. Boettiger, Loop stacking organizes genome folding from TADs to chromosomes. *Mol. Cell* **83**, 1377–1392.e6 (2023).
33. J. Otterstrom, A. Castells-Garcia, C. Vicario, P. A. Gomez-Garcia, M. P. Cosma, M. Lakadamyali, Super-resolution microscopy reveals how histone tail acetylation affects DNA compaction within nucleosomes in vivo. *Nucleic Acids Res.* **47**, 8470–8484 (2019).
34. M. A. Ricci, C. Manzo, M. F. García-Parajo, M. Lakadamyali, M. P. Cosma, Chromatin fibers are formed by heterogeneous groups of nucleosomes in vivo. *Cell* **160**, 1145–1158 (2015).
35. T. Nozaki, S. Shinkai, S. Ide, K. Higashi, S. Tamura, M. A. Shimazoe, M. Nakagawa, Y. Suzuki, Y. Okada, M. Sasai, S. Onami, K. Kurokawa, S. Iida, K. Maeshima, Condensed but liquid-like domain organization of active chromatin regions in living human cells. *Sci. Adv.* **9**, eadf1488 (2023).
36. Y. Li, V. Agrawal, R. K. A. Virk, E. Roth, W. S. Li, A. Eshein, J. Frederick, K. Huang, L. Almassalha, R. Bleher, M. A. Carignano, I. Szleifer, V. P. Dravid, V. Backman, Analysis of three-dimensional chromatin packing domains by chromatin scanning transmission electron microscopy (ChromSTEM). *Sci. Rep.* **12**, 12198 (2022).
37. L. A. Mirny, The fractal globule as a model of chromatin architecture in the cell. *Chromosome Res.* **19**, 37–51 (2011).
38. G. Fudenberg, G. Getz, M. Meyerson, L. A. Mirny, High order chromatin architecture shapes the landscape of chromosomal alterations in cancer. *Nat. Biotechnol.* **29**, 1109–1113 (2011).
39. K. E. Polovnikov, M. Gherardi, M. Cosentino-Lagomarsino, M. V. Tamm, Fractal folding and medium viscoelasticity contribute jointly to chromosome dynamics. *Phys. Rev. Lett.* **120**, 088101 (2018).
40. M. V. Tamm, L. I. Nazarov, A. A. Gavrilov, A. V. Chertovich, Anomalous diffusion in fractal globules. *Phys. Rev. Lett.* **114**, 178102 (2015).
41. G. Forte, A. Buckle, S. Boyle, D. Marenduzzo, N. Gilbert, C. A. Brackley, Transcription modulates chromatin dynamics and locus configuration sampling. *Nat. Struct. Mol. Biol.* **30**, 1275–1285 (2023).

42. K. Huang, Y. Li, A. R. Shim, R. K. A. Virk, V. Agrawal, A. Eshein, R. J. Nap, L. M. Almassalha, V. Backman, I. Szleifer, Physical and data structure of 3D genome. *Sci. Adv.* **6**, eaay4055 (2020).
43. T.-H. S. Hsieh, C. Cattoglio, E. Slobodyanyuk, A. S. Hansen, X. Darzacq, R. Tjian, Enhancer–promoter interactions and transcription are largely maintained upon acute loss of CTCF, cohesin, WAPL or YY1. *Nat. Genet.* **54**, 1919–1932 (2022).
44. M. Gabriele, H. B. Brandão, S. Grosse-Holz, A. Jha, G. M. Dailey, C. Cattoglio, T.-H. S. Hsieh, L. Mirny, C. Zechner, A. S. Hansen, Dynamics of CTCF- and cohesin-mediated chromatin looping revealed by live-cell imaging. *Science* **376**, 496–501 (2022).
45. Y. Liu, J. Dekker, CTCF–CTCF loops and intra-TAD interactions show differential dependence on cohesin ring integrity. *Nat. Cell Biol.* **24**, 1516–1527 (2022).
46. M. A. Carignano, M. Kroeger, L. M. Almassalha, V. Agrawal, W. S. Li, E. M. Pujadas-Liwag, R. J. Nap, V. Backman, I. Szleifer, Local volume concentration, packing domains, and scaling properties of chromatin. *eLife* **13**, RP97604 (2024).
47. H. Matsuda, G. G. Putzel, V. Backman, I. Szleifer, Macromolecular crowding as a regulator of gene transcription. *Biophys. J.* **106**, 1801–1810 (2014).
48. G. G. Putzel, M. Tagliazucchi, I. Szleifer, Nonmonotonic diffusion of particles among larger attractive crowding spheres. *Phys. Rev. Lett.* **113**, 138302 (2014).
49. K. Maeshima, K. Kaizu, S. Tamura, T. Nozaki, T. Kokubo, K. Takahashi, The physical size of transcription factors is key to transcriptional regulation in chromatin domains. *J. Phys. Condens. Matter* **27**, 064116 (2015).
50. J. Jumper, R. Evans, A. Pritzel, T. Green, M. Figurnov, O. Ronneberger, K. Tunyasuvunakool, R. Bates, A. Žídek, A. Potapenko, A. Bridgland, C. Meyer, S. A. A. Kohl, A. J. Ballard, A. Cowie, B. Romera-Paredes, S. Nikolov, R. Jain, J. Adler, T. Back, S. Petersen, D. Reiman, E. Clancy, M. Zielinski, M. Steinegger, M. Pacholska, T. Berghammer, S. Bodenstein, D. Silver, O. Vinyals, A. W. Senior, K. Kavukcuoglu, P. Kohli, D. Hassabis, Highly accurate protein structure prediction with AlphaFold. *Nature* **596**, 583–589 (2021).
51. R. K. A. Virk, W. Wu, L. M. Almassalha, G. M. Bauer, Y. Li, D. VanDerway, J. Frederick, D. Zhang, A. Eshein, H. K. Roy, I. Szleifer, V. Backman, Disordered chromatin packing regulates phenotypic plasticity. *Sci. Adv.* **6**, eaax6232 (2020).
52. L. M. Almassalha, A. Tiwari, P. T. Ruhoff, Y. Stypula-Cyrus, L. Cherkezyan, H. Matsuda, M. A. Dela Cruz, J. E. Chandler, C. White, C. Maneval, H. Subramanian, I. Szleifer, H. K. Roy, V. Backman, The global relationship between chromatin physical topology, fractal structure, and gene expression. *Sci. Rep.* **7**, 41061 (2017).
53. L. M. Almassalha, G. M. Bauer, W. Wu, L. Cherkezyan, D. Zhang, A. Kendra, S. Gladstein, J. E. Chandler, D. VanDerway, B.-L. L. Seagle, A. Ugolkov, D. D. Billadeau, T. V. O'Halloran, A. P. Mazar, H. K. Roy, I. Szleifer, S. Shahabi, V. Backman, Macrogenomic engineering via modulation of the scaling of chromatin packing density. *Nat. Biomed. Eng.* **1**, 902–913 (2017).
54. C. Tan, S. Saurabh, M. P. Bruchez, R. Schwartz, P. LeDuc, Molecular crowding shapes gene expression in synthetic cellular nanosystems. *Nat. Nanotechnol.* **8**, 602–608 (2013).
55. Y. Lorch, R. D. Kornberg, B. Maier-Davis, Role of the histone tails in histone octamer transfer. *Nucleic Acids Res.* **51**, 3671–3678 (2023).
56. K. Maeshima, T. Matsuda, Y. Shindo, H. Imamura, S. Tamura, R. Imai, S. Kawakami, R. Nagashima, T. Soga, H. Noji, K. Oka, T. Nagai, A transient rise in free Mg^{2+} ions released from ATP-Mg hydrolysis contributes to mitotic chromosome condensation. *Curr. Biol.* **28**, 444–451.e6 (2018).
57. A. D. Stephens, P. Z. Liu, V. Kandula, H. Chen, L. M. Almassalha, C. Herman, V. Backman, T. O'Halloran, S. A. Adam, R. D. Goldman, E. J. Banigan, J. F. Marko, Physicochemical mechanotransduction alters nuclear shape and mechanics via heterochromatin formation. *Mol. Biol. Cell* **30**, 2320–2330 (2019).
58. K. Nishimura, T. Fukagawa, H. Takisawa, T. Kakimoto, M. Kanemaki, An auxin-based degron system for the rapid depletion of proteins in nonplant cells. *Nat. Methods* **6**, 917–922 (2009).
59. A. Yesbolatova, Y. Saito, N. Kitamoto, H. Makino-Itou, R. Ajima, R. Nakano, H. Nakaoka, K. Fukui, K. Gamo, Y. Tominari, H. Takeuchi, Y. Saga, K. Hayashi, M. T. Kanemaki, The auxin-inducible degron 2 technology provides sharp degradation control in yeast, mammalian cells, and mice. *Nat. Commun.* **11**, 5701 (2020).
60. O. Bensaude, Inhibiting eukaryotic transcription: Which compound to choose? How to evaluate its activity? *Transcription* **2**, 103–108 (2011).
61. S. Gladstein, L. M. Almassalha, L. Cherkezyan, J. E. Chandler, A. Eshein, A. Eid, D. Zhang, W. Wu, G. M. Bauer, A. D. Stephens, S. Morochnik, H. Subramanian, J. F. Marko, G. A. Ameer, I. Szleifer, V. Backman, Multimodal interference-based imaging of nanoscale structure and macromolecular motion uncovers UV induced cellular paroxysm. *Nat. Commun.* **10**, 1652 (2019).
62. L. M. Almassalha, G. M. Bauer, J. E. Chandler, S. Gladstein, L. Cherkezyan, Y. Stypula-Cyrus, S. Weinberg, D. Zhang, P. Thusgaard Ruhoff, H. K. Roy, H. Subramanian, N. S. Chandel, I. Szleifer, V. Backman, Label-free imaging of the native, living cellular nanoarchitecture using partial-wave spectroscopic microscopy. *Proc. Natl. Acad. Sci. U.S.A.* **113**, E6372–E6381 (2016).
63. A. Castells-Garcia, I. Ed-daoui, E. González-Almela, C. Vicario, J. Ottestrom, M. Lakadamyali, M. V. Neguembor, M. P. Cosma, Super resolution microscopy reveals how elongating RNA polymerase II and nascent RNA interact with nucleosome clutches. *Nucleic Acids Res.* **50**, 175–190 (2022).
64. S.-J. Heo, S. Thakur, X. Chen, C. Loebel, B. Xia, R. McBeath, J. A. Burdick, V. B. Shenoy, R. L. Mauck, M. Lakadamyali, Aberrant chromatin reorganization in cells from diseased fibrous connective tissue in response to altered chemomechanical cues. *Nat. Biomed. Eng.* **7**, 177–191 (2023).
65. E. A. Bowman, W. G. Kelly, RNA polymerase II transcription elongation and Pol II CTD Ser2 phosphorylation: A tail of two kinases. *Nucleus* **5**, 224–236 (2014).
66. T. Yu, Y. Wang, Q. Hu, W. Wu, Y. Wu, W. Wei, D. Han, Y. You, N. Lin, N. Liu, The EZH2 inhibitor GSK343 suppresses cancer stem-like phenotypes and reverses mesenchymal transition in glioma cells. *Oncotarget* **8**, 98348–98359 (2017).
67. B. C. Hitz, J.-W. Lee, O. Jolanki, M. S. Kagda, K. Graham, P. Sud, I. Gabdank, J. S. Strattan, C. A. Sloan, T. Dreszer, L. D. Rowe, N. R. Podduturi, V. S. Malladi, E. T. Chan, J. M. Davidson, M. Ho, S. Miyasato, M. Simison, F. Tanaka, Y. Luo, I. Whaling, E. L. Hong, B. T. Lee, R. Sandstrom, E. Rynes, J. Nelson, A. Nishida, A. Ingersoll, M. Buckley, M. Frerker, D. S. Kim, N. Boley, D. Trout, A. Dobin, S. Rahmanian, D. Wyman, G. Balderrama-Gutierrez, F. Reese, N. C. Durand, O. Dudchenko, D. Weisz, S. S. P. Rao, A. Blackburn, D. Gkountaroulis, M. Sadr, M. Olshansky, Y. Eliaz, D. Nguyen, I. Bochkov, M. S. Shamim, R. Mahajan, E. Aiden, T. Gingeras, S. Heath, M. Hirst, W. J. Kent, A. Kundaje, A. Mortazavi, B. Wold, J. M. Cherry, The ENCODE uniform analysis pipelines. bioRxiv 535623 [Preprint] (2023). https://doi.org/10.1101/2023.04.04.535623.
68. ENCODE Project Consortium, An integrated encyclopedia of DNA elements in the human genome. *Nature* **489**, 57–74 (2012).
69. Y. Luo, B. C. Hitz, I. Gabdank, J. A. Hilton, M. S. Kagda, B. Lam, Z. Myers, P. Sud, J. Jou, K. Lin, U. K. Baymuradov, K. Graham, C. Litton, S. R. Miyasato, J. S. Strattan, O. Jolanki, J.-W. Lee, F. Y. Tanaka, P. Adenekan, E. O'Neill, J. M. Cherry, New developments on the Encyclopedia of DNA Elements (ENCODE) data portal. *Nucleic Acids Res.* **48**, D882–D889 (2020).
70. R. U. Pathak, M. Soujanya, R. K. Mishra, Deterioration of nuclear morphology and architecture: A hallmark of senescence and aging. *Ageing Res. Rev.* **67**, 101264 (2021).
71. A. Brandt, G. Krohne, J. Großhans, The farnesylated nuclear proteins KUGELKERN and LAMIN B promote aging-like phenotypes in *Drosophila* flies. *Aging Cell* **7**, 541–551 (2008).
72. J. Kang, D. I. Benjamin, S. Kim, J. S. Salvi, G. Dhaliwal, R. Lam, A. Goshayeshi, J. O. Brett, L. Liu, T. A. Rando, Depletion of SAM leading to loss of heterochromatin drives muscle stem cell ageing. *Nat. Metab.* **6**, 153–168 (2024).
73. J.-H. Lee, E. W. Kim, D. L. Croteau, V. A. Bohr, Heterochromatin: An epigenetic point of view in aging. *Exp. Mol. Med.* **52**, 1466–1474 (2020).
74. D. Nicetto, K. S. Zaret, Role of H3K9me3 heterochromatin in cell identity establishment and maintenance. *Curr. Opin. Genet. Dev.* **55**, 1–10 (2019).
75. E. Benz, A. Pinel, C. Guillet, F. Capel, B. Pereira, M. De Antonio, M. Pouget, A. J. Cruz-Jentoft, D. Eglseer, E. Topinkova, R. Barazzoni, F. Rivadeneira, M. A. Ikram, M. Steur, T. Voortman, J. D. Schoufour, P. J. M. Weijs, Y. Boirie, Sarcopenia and sarcopenic obesity and mortality among older people. *JAMA Netw. Open* **7**, e243604 (2024).
76. C. Beaudart, C. Demonceau, J. Reginster, M. Locquet, M. Cesari, A. J. Cruz Jentoft, O. Bruyère, Sarcopenia and health-related quality of life: A systematic review and meta-analysis. *J. Cachexia. Sarcopenia Muscle* **14**, 1228–1243 (2023).
77. J. Xu, C. S. Wan, K. Ktoris, E. M. Reijnierse, A. B. Maier, Sarcopenia is associated with mortality in adults: A systematic review and meta-analysis. *Gerontology* **68**, 361–376 (2022).
78. Z. Yang, K. L. MacQuarrie, E. Analau, A. E. Tyler, F. J. Dilworth, Y. Cao, S. J. Diede, S. J. Tapscott, MyoD and E-protein heterodimers switch rhabdomyosarcoma cells from an arrested myoblast phase to a differentiated state. *Genes Dev.* **23**, 694–707 (2009).
79. Y. Cao, Z. Yao, D. Sarkar, M. Lawrence, G. J. Sanchez, M. H. Parker, K. L. MacQuarrie, J. Davison, M. T. Morgan, W. L. Ruzzo, R. C. Gentleman, S. J. Tapscott, Genome-wide MyoD binding in skeletal muscle cells: A potential for broad cellular reprogramming. *Dev. Cell* **18**, 662–674 (2010).
80. Y. Nabeshima, K. Hanaoka, M. Hayasaka, E. Esuml, S. Li, I. Nonaka, Y. Nabeshima, Myogenin gene disruption results in perinatal lethality because of severe muscle defect. *Nature* **364**, 532–535 (1993).
81. J. M. Hernández-Hernández, E. G. García-González, C. E. Brun, M. A. Rudnicki, The myogenic regulatory factors, determinants of muscle development, cell identity and regeneration. *Semin. Cell Dev. Biol.* **72**, 10–18 (2017).
82. V. R. Kedlian, Y. Wang, T. Liu, X. Chen, L. Bolt, C. Tudor, Z. Shen, E. S. Fasouli, E. Prigmore, V. Kleshchevnikov, J. P. Pett, T. Li, J. E. G. Lawrence, S. Perera, M. Prete, N. Huang, Q. Guo, X. Zeng, L. Yang, K. Polański, N.-J. Chipampe, M. Dabrowska, X. Li, O. A. Bayraktar, M. Patel, N. Kumasaka, K. T. Mahbubani, A. P. Xiang, K. B. Meyer, K. Saeb-Parsy, S. A. Teichmann, H. Zhang, Human skeletal muscle aging atlas. *Nat. Aging* , 727–744 (2024).
83. W. Schwarzer, N. Abdennur, A. Goloborodko, A. Pekowska, G. Fudenberg, Y. Loe-Mie, N. A. Fonseca, W. Huber, C. H. Haering, L. Mirny, F. Spitz, Two independent modes of chromatin organization revealed by cohesin removal. *Nature* **551**, 51–56 (2017).
84. L. P. Kaelbling, M. L. Littman, A. W. Moore, Reinforcement learning: A survey. *J Artif Intell Res* **4**, 237–285 (1996).

85. I. Mitroulis, K. Ruppova, B. Wang, L.-S. Chen, M. Grzybek, T. Grinenko, A. Eugster, M. Troullinaki, A. Palladini, I. Kourtzelis, A. Chatzigeorgiou, A. Schlitzer, M. Beyer, L. A. B. Joosten, B. Isermann, M. Lesche, A. Petzold, K. Simons, I. Henry, A. Dahl, J. L. Schultze, B. Wielockx, N. Zamboni, P. Mirtschink, Ü. Coskun, G. Hajishengallis, M. G. Netea, T. Chavakis, Modulation of myelopoiesis progenitors is an integral component of trained immunity. *Cell* **172**, 147–161.e12 (2018).
86. V. Parreno, V. Loubiere, B. Schuettengruber, L. Fritsch, C. C. Rawal, M. Erokhin, B. Győrffy, D. Normanno, M. Di Stefano, J. Moreaux, N. L. Butova, I. Chiolo, D. Chetverina, A.-M. Martinez, G. Cavalli, Transient loss of polycomb components induces an epigenetic cancer fate. *Nature* **629**, 688–696 (2024).
87. E. R. H. Walter, M. A. Fox, D. Parker, J. A. G. Williams, Enhanced selectivity for Mg^{2+} with a phosphinate-based chelate: APDAP *versus* APTRA. *Dalton Trans.* **47**, 1879–1887 (2018).
88. N. C. Durand, M. S. Shamim, I. Machol, S. S. P. Rao, M. H. Huntley, E. S. Lander, E. L. Aiden, Juicer provides a one-click system for analyzing loop-resolution Hi-C experiments. *Cell Syst.* **3**, 95–98 (2016).
89. R. H. van der Weide, T. van den Brand, J. H. I. Haarhuis, H. Teunissen, B. D. Rowland, E. de Wit, Hi-C analyses with GENOVA: A case study with cohesin variants. *NAR Genom. Bioinform.* **3**, lqab040 (2021).
90. N. Abdennur, L. A. Mirny, Cooler: Scalable storage for Hi-C data and other genomically labeled arrays. *Bioinformatics* **36**, 311–316 (2020).
91. N. Abdennur, S. Abraham, G. Fudenberg, I. M. Flyamer, A. A. Galitsyna, A. Goloborodko, M. Imakaev, B. A. Oksuz, S. V. Venev, Y. Xiao, Cooltools: Enabling high-resolution Hi-C analysis in Python. *PLOS Comput. Biol.* **20**, e1012067 (2024).
92. M. Ovesný, P. Křížek, J. Borkovec, Z. Švindrych, G. M. Hagen, ThunderSTORM: A comprehensive ImageJ plug-in for PALM and STORM data analysis and super-resolution imaging. *Bioinformatics* **30**, 2389–2390 (2014).
93. W. M. Brown, M. K. Petersen, S. J. Plimpton, G. S. Grest, Liquid crystal nanodroplets in solution. *J. Chem. Phys.* **130**, 044901 (2009).
94. A. P. Thompson, H. M. Aktulga, R. Berger, D. S. Bolintineanu, W. M. Brown, P. S. Crozier, P. J. in't Veld, A. Kohlmeyer, S. G. Moore, T. D. Nguyen, R. Shan, M. J. Stevens, J. Tranchida, C. Trott, S. J. Plimpton, LAMMPS—A flexible simulation tool for particle-based materials modeling at the atomic, meso, and continuum scales. *Comput. Phys. Commun.* **271**, 108171 (2022).

Acknowledgments: ChatGPT 4.0 was used to assist in calculating the radius of gyration of proteins. No AI tools or external reviewers were used for conceptualization, writing, synthesis, or direct analysis of results. Philanthropic support was received from R. and K. Goldman, the Christina Carinato Charitable Foundation, M. E. Holliday, I. Schneider, and D. Sachs. Computational analysis of Hi-C data was supported in part through the computational resources and staff contributions provided by the Genomics Compute Cluster, which is jointly supported by the Feinberg School of Medicine, the Center for Genetic Medicine, and Feinberg's Department of Biochemistry and Molecular Genetics, the Office of the Provost, the Office for Research, and Northwestern Information Technology. The Genomics Compute Cluster is part of Quest, Northwestern University's high-performance computing facility, with the purpose to advance research in genomics. We appreciate the support from the ENCODE Consortium in the generation and dissemination of publicly available datasets. We specifically want to thank the labs of B. Bernstein, T. Gingeras, P. Farnham, R. Myers, and J. Stamatoyannopoulo for the generation and publication of the data used within this manuscript. This work made use of the BioCryo facility (RRID:SCR_021288) of Northwestern University's NUANCE Center, which has received support from the SHyNE Resource (NSF ECCS-2025633), the IIN, and Northwestern's MRSEC program (NSF DMR-2308691). **Funding:** This work was supported by the National Science Foundation grant EFMA-1830961 (E.P.L., M.C., I.S., and V.B.), National Science Foundation grant EFMA-1830969 (E.P.L. and V.B.), National Science Foundation grant ECCS-2025633 (V.D.), National Science Foundation grant DMR-2308691 (V.D.), National Institutes of Health grant R01CA228272 (W.S.L., T.K., I.S., and V.B.), National Institutes of Health grant U54 CA268084 (W.S.L., L.M.C., L.M.A., E.P.L., T.K., K.L.M., M.C., I.S., and V.B.), National Institutes of Health grant U54 CA261694 (L.M.C., V.S., and V.B.), NIH Training Grant T32AI083216 (L.M.A.), NIH Training Grant T32GM132605 (T.K., L.M.C., and V.B.), Hyundai Hope on Wheels Hope Scholar Grant (K.L.M.), CURE Childhood Cancer Early Investigator Grant (K.L.M.), Alex's Lemonade Stand Foundation "A" award grant (K.L.M.), Ann and Robert H. Lurie Children's Hospital of Chicago under the Molecular and Translational Cancer Biology Neighborhood (K.L.M.), Northwestern University Starzl Scholar Award (L.M.A.), and National Institutes of Health National Center for Advancing Translational Sciences KL2TR001424 (K.L.M.). **Author contributions:** Conceptualization: V.D., E.P.L., L.M.C., V.B., T.K., I.S., L.M.A., M.C., P.C.G., P.S., K.I.M., and J.F. Writing—original draft: E.P.L., I.S., L.M.A., and K.I.M. Writing—review and editing: V.D., E.P.L., R.K., I.C.Y., M.K., R.N., C.L.D., L.M.C., V.B., T.K., I.S., W.S.L., K.L.M., M.C., P.C.G., P.S., K.I.M., and J.F. Methodology: V.D., C.L.D., L.M.C., V.B., I.S., M.K., L.M.A., M.C., P.C.G., P.S., and J.F. Resources: V.D., M.K., L.M.C., V.B., I.S., L.M.A., and R.G. Funding acquisition: V.D., V.B., I.S., L.M.A., and K.L.M. Supervision: V.D., V.B., I.S., and L.M.A. Project administration: V.D., V.B., I.S., and L.M.A. Investigation: E.P.L., R.K., C.L.D., N.A., L.M.C., T.K., I.S., W.S.L., K.L.M., L.M.A., R.G., P.C.G., J.A.P., K.I.M., and J.F. Validation: E.P.L., R.K., L.M.C., V.B., I.S., M.K., L.M.A., R.G., K.I.M., and J.F. Formal analysis: E.P.L., R.K., I.C.Y., R.N., C.L.D., N.A., V.B., T.K., I.S., M.K., W.S.L., L.M.A., M.C., R.G., P.C.G., A.S., P.S., and J.F. Visualization: E.P.L., I.C.Y., C.L.D., N.A., L.M.C., I.S., W.S.L., L.M.A., M.C., P.C.G., K.M., and J.F. Software: R.N., N.A., L.M.C., I.S., M.K., M.C., R.G., A.S., P.S., and J.F. Data curation: L.M.C., I.S., L.M.A., and J.F. **Competing interests:** The authors declare that they have no competing interests. **Data and materials availability:** All of the data, analysis software, and relevant materials have been uploaded to the following locations. ChIP-seq data were obtained from the ENCODE Consortium (*67*–*69*) with the relevant accession numbers posted in the Supplementary Materials in table S2. All data needed to evaluate the conclusions in the paper are present in the paper and/or the Supplementary Materials. Compiled data to regenerate the figures are available on Dryad at DOI: 10.5061/dryad.b8gtht7p0 and genomics data at GEO with accession numbers GSE279166 and GSE283236.

Submitted 24 May 2024
Accepted 4 December 2024
Published 10 January 2025
10.1126/sciadv.adq6652